Eur. Phys. J. A **1**, 407–426 (1998)

THE EUROPEAN
PHYSICAL JOURNAL A

Low-energy fission investigated in reactions of 750 AMeV ^{238}U-ions on ^{208}Pb. II: Isotopic distributions

C. Donzaud[1,2], S. Czajkowski[2,3], P. Armbruster[2], M. Bernas[1], C. Böckstiegel[5], Ph. Dessagne[4], H. Geissel[2], E. Hanelt[5], A. Heinz[5], C. Kozhuharov[2], Ch. Miehé[4], G. Münzenberg[2], M. Pfützner[6], W. Schwab[2], C. Stéphan[1], K. Sümmerer[2], L. Tassan-Got[1], B. Voss[2,5]

[1] IPN Orsay, IN2P3, CNRS, F-91406 Orsay Cedex, France
[2] GSI Darmstadt, HGF, Postfach 110552, D-64220 Darmstadt, Germany
[3] CENBG Bordeaux-Gradignan, IN2P3, CNRS, BP 120, F-33170 Gradignan Cedex, France
[4] IReS Strasbourg, IN2P3, CNRS, F-67037 Strasbourg Cedex, France
[5] TH Darmstadt, Institut für Kernphysik, Schlossgartenstrasse 9, D-64289 Darmstadt, Germany
[6] IFD, University Warsaw, Pl-00681 Warsaw, Hoza 69, Poland

Received: 14 July 1997 / Revised version: 6 October 1997
Communicated by V. Metag

Abstract. Projectile fission of 750 AMeV ^{238}U-ions interacting with a Pb target was studied by means of the spectrometer FRS, GSI-Darmstadt. One of the two fission fragments was detected with a transmission of few percent and identified in mass and charge. Low-energy fission (E^* <25 MeV) events were selected by their magnetic rigidity. Whereas the production of asymmetric fission events is dominated by the GDR excitation, very asymmetric fission and symmetric fission take place after a GQR or DGDR excitation or after a nuclear interaction. Cross sections of more than 250 isotopes were measured. Isotopic distributions of low-energy fission were reconstructed for elements from Se to Te. The fission modes SI, SII and SL were clearly shown in these distributions and in the mass and TKE distributions. Charge polarization and mass dispersion were deduced for each fission mode. Finally, the characteristics of the low-energy fission process explain the production rates of neutron-rich species.

PACS. 25.85.-W Fission reactions

1 Introduction

When a nucleus undergoes fission, a significant neutron-excess is observed in the two fragments if the fissioning nucleus is kept not too highly excited. Under this condition, fission remains the most efficient process to produce neutron-rich isotopes. Up to recently, target fission only could be investigated. The acceleration of ^{238}U to relativistic energies by the SIS, GSI-Darmstadt, allowed to investigate the fission of U as a projectile [1–4]. This paper is devoted to the low-energy fission component measured in the reaction of 750 AMeV ^{238}U impinging on a Pb target. Fifty new neutron-rich nuclei were identified in this experiment [5]. The element distribution of the low-energy fission events, already published, shows the characteristics of an asymmetric fission process [6]. The present investigation concentrates on the isotopic distributions of fission fragments with atomic numbers ranging from Ga to Te. Fully stripped fragments were identified in charge, mass and velocity by means of the FRS spectrometer equipped with standard detection. Independent yields Y(Z,A) were deduced for about 250 nuclei. For the first time, fragments are isotopically resolved over the full fission fragment domain using in-flight separator techniques.

When U fission takes place after electromagnetic interaction, ie. at large impact parameters, the fissioning system is still an U isotope. At impact parameters allowing nuclear contact, fission of lighter fissile systems is observed. In this case, the high excitation energy deposited in the system (about 27 MeV per abraded nucleon [7]) is released by evaporation of pre-fission nucleons, mostly neutrons. The fission process itself is occurring at the end of the de-excitation chain [8]. The low-energy fission process (E^* <25 MeV) results from EM or soft nuclear interactions. Since the probability for interactions via the electromagnetic field increases with incident energy and a dominance of the E1 excitation is expected, GDR excitation ($\simeq$ 12 MeV) becomes the main path towards low-energy fission. Among the 13.4±1.0 b total reaction cross section [2], low-energy fission contributes to 2.1±0.2 b in the reaction studied [6]. It is noteworthy that this low-energy process uses only a tiny part ($\sim 2 \times 10^{-4}$) of the huge energy available in the center of mass of the system.

The production yields of fission products in the valley of the mass distribution are known for a long time to reflect with high sensitivity the excitation energy in the fissioning system [9]. As a successful working hypothesis Turkevich and Niday [10] proposed two distinct fission modes, an asymmetric and a symmetric mode. Later applying the Strutinski-procedure Wilkins et al [11] developed a static scission-point model. They found besides the symmetric mode in the asymmetric break-up two subchannels, a channel of high kinetic energy with a spherical heavy fragment (Z≃50, N≃82) and a channel of lower kinetic energy with a deformed heavy fragment (N≃88). The model was refined by Brosa et al [12] and presently at least three break-ups, the symmetric mode (SL) and the two asymmetric channels (SII and SI) are established for the lighter actinides. In the present analysis, isotopic distributions corresponding to low-energy fission processes are determined. Compared to the well-known fission processes induced by low energy neutrons and photons, the modes appear in unusual ratios due to higher excitation energies. For the first time the three different fission modes are clearly exhibited in isotopic distributions. The main characteristics of the symmetric and asymmetric fission components are deduced giving a consistent picture of the low-energy fission process. This helps us to understand the high production rate of neutron-rich nuclei.

2 Experimental techniques

2.1 Experimental set-up

A beam of 2×10^5 ^{238}U ions/s accelerated up to 750 AMeV by the heavy-ion synchrotron SIS was impinging on a 1.26 g/cm^2 Pb target located at the entrance focus of the fragment separator FRS. The duty cycle of the beam was 1 pulse every 4 s, the pulse length being 80 ms on average. The size of the beam spot on the target was measured with beam-profile grids to be less than 2 mm (FWHM) in the horizontal direction and 3 mm in the vertical direction. The beam intensity was measured with a secondary-electron current monitor SEETRAM [13]. It was calibrated by comparing the measured electric current with the counting rate of individual particles registered by a scintillation counter at moderate counting rates. The accuracy of the beam intensity determined by this method is estimated to be ±7% [14].

The reaction products were analyzed with the FRS which was operated in the achromatic mode [15] (Fig. 1). A wide range of magnetic rigidity values of the fragments ($B\rho$) was explored on both sides of $B\rho_0$, the magnetic rigidity of the projectile. Backward-emitted fragments from low-energy fission, fragments from high-energy fission, and fragmentation products populate the magnetic rigidity domain with $\frac{B\rho}{B\rho_0} < 1$. Only forward-emitted fragments from low-energy fission are detected at $\frac{B\rho}{B\rho_0} > 1$ [6]. We concentrate here on the events accumulated in 8 magnetic settings from 1.0064 to 1.1126 Tesla in the first half of the spectrometer. For settings close to the magnetic field of the primary beam, 1 Tesla, a slit was set behind the first magnetic dipole in order to limit the counting rate.

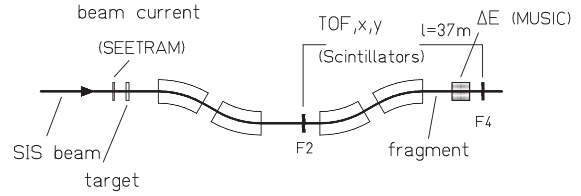

Fig. 1. Schematic drawing of the FRS operating in the achromatic mode. Fragments are identified in the second stage of the spectrometer by a ΔE-ToF-$B\rho$ method by means of two plastic scintillators set in the intermediate and final focal planes and a MUSIC chamber

As the kinematics of the low-energy fission process and the transmission of isotopes through the spectrometer are already described [6], we only give a quick overview here. In the ^{238}U frame, fission fragments are emitted back to back with an angular distribution which is isotropic to the first order. For a given element the resulting spherical shell of momenta is converted to a cone of vectors ending on a shell of an ellipsoid in the laboratory system (see Fig. 2). As the opening angle of this cone (±30 mr for Zr) is larger than the ±15 mr angular acceptance of the FRS, only fragments emitted either forward or backward are transmitted (filled areas). Moreover, the ±1% momentum acceptance of the FRS selects only one of the two fission fragments which are widely separated in momentum space.

The cuts in the momentum phase space induced by the spectrometer appear in Fig. 3 which shows the $\beta\gamma$-distribution of forward and backward emitted isotopes coming from a low-energy fission process for Zr and Te. The displayed Gaussian distributions with high $\beta\gamma$-values correspond to magnetic settings with $\frac{B\rho}{B\rho_0} > 1$. The analysis of these curves will be discussed later. Distributions centered at low $\beta\gamma$-values come from few explored measurements at $\frac{B\rho}{B\rho_0} < 1$. For Zr and Te it was checked that the average $\beta\gamma$-value of the measured centroids in the forward and backward directions give the expected $\beta\gamma$-value

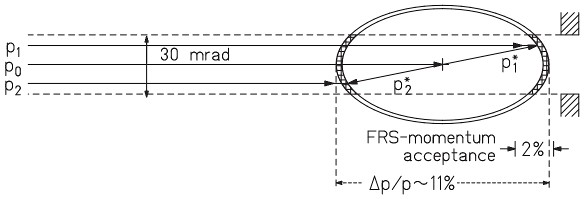

Fig. 2. Momentum phase space diagram calculated for the Zr fission fragments. $\mathbf{p}_0$ is the momentum of the incident ^{238}U in the laboratory system with β_0=0.83. $\mathbf{p}_1^*$=-$\mathbf{p}_2^*$ are the momenta of a pair of fission products in the center of mass which become $\mathbf{p}_1$ and $\mathbf{p}_2$ in the laboratory system. Within the 2% momentum acceptance and the 30 mrad angular acceptance of the spectrometer, only the momenta ending on the *filled areas* are transmitted

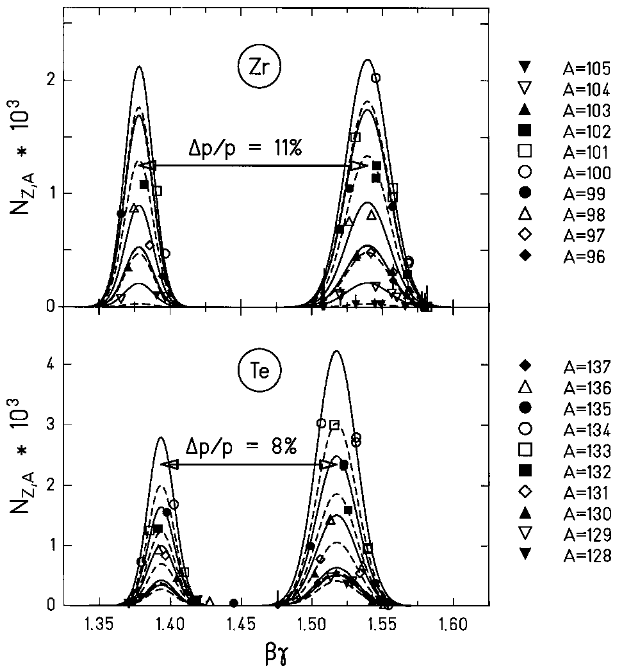

Fig. 3. Measured $\beta\gamma$-distributions of Zr and Te isotopes emitted in the forward and backward directions in the center of mass system. The *points* are measured rates corresponding to velocities determined in the middle of the target. The *curves* are associated fits

of the incident beam in the middle of the target with a precision better than 1%. Moreover, the difference $\Delta p/p$ between the forward and backward fragments is found to 11% for Zr isotopes and 8% for Te isotopes as expected from the calculation described in Ref. [6].

The use of a thick target allows a simultaneous transmission of 3 or 4 isotopes of each element through the spectrometer instead of 2 expected from the momentum acceptance. The transmission of isotopes was simulated by the Monte-Carlo code MOCADI developed for the fragmentation mechanism [16] to simulate the transport through the FRS and atomic interactions with target and degraders. To make this code applicable for fission, an isotropic angular distribution was assumed and the center of mass kinetic energy of the fission products taken from ^{235}U thermal neutron-induced fission was introduced; an assumption confirmed by the measured velocity distributions (see Fig. 6). The transmission values along the central trajectory T_{max} extend from 1.6% for Ni isotopes to 4.8% for Te isotopes. To first order for each element, they are independent of the mass of the isotopes; this is supported by the equality of the observed mean velocities in an isotopic series (see Fig. 5). With the FRS tuned on the light group of fission products (Z=40), elements between Ni and Te were fully transmitted. The uncertainty of around 10 % on transmission absolute values is a possible source of systematic error on cross sections values.

2.2 Identification of fragments

Fragments were identified event-by-event with respect to nuclear charge and mass by a ΔE-ToF-$B\rho$ method in the second stage of the FRS (Fig. 1). Energy-loss (ΔE) measurements were performed at the final focal plane by a four-stage ionization chamber MUSIC [17]. For the domain investigated here ($Z \leq 52$) the nuclear charge Z is equal to the ionic charge q calculated from $\Delta E = (\prod_{i=1}^{4} \Delta E_i)^{\frac{1}{4}}$ where ΔE_i is measured in the ith part of the chamber. After being corrected for its velocity dependence, the ΔE signal gives a Z-resolving power of 130. The absolute Z calibration was insured from the known fission pattern: the reconstructed Z-distribution over all settings with $\frac{B\rho}{B\rho_0} > 1$ exhibits the clear enhancement of the Zr/Te pair [6].

The time-of-flight (ToF) and the flight path of fragments were determined by two position-sensitive scintillation detectors [18] mounted at the intermediate and final focal planes. They are 5 mm thick each and cover a 200 mm (horizontally) × 80 mm (vertically) area. Energy losses in the scintillator set in the midplane, measured using the primary beam, were taken into account to calculate the rigidity in the second half of the spectrometer.

The horizontal positions in the scintillators were deduced from $log(E_R/E_L)$ were E_R and E_L are the photomultiplier signals taken at both ends of the detectors. The positions were calibrated by means of multi-wire proportional chambers [19] which were removed from the beam during the main experiment. The location resolution of the scintillators reached about 4 mm (FWHM). The length of the flight path between the two focal planes was determined from the horizontal position in the scintillation detectors and from the angle of the trajectory at the exit of the FRS. This angle was deduced from the horizontal positions measured by the electron drift-times in the first and fourth stage of the MUSIC.

The time-of-flight was determined as the mean value $(\mathrm{ToF}_R + \mathrm{ToF}_L)/2$ where ToF_R (ToF_L) is the time difference between the two scintillators signals registered at the right (left) end. It was calibrated by means of several U energies obtained by introducing degraders of different thicknesses in the intermediate focal plane. A time resolution of 200 ps over a flight time of 150 ns was achieved.

The $Z - \beta\gamma$ scatter-plot of fission fragments observed at $B\rho = 1.04 B\rho_0$ is displayed in Fig. 4. The fragments are unambiguously separated with a mass resolution of 250. The background is estimated to be less than 1 event per hour in the low counting rate region. This is verified at the high $B\rho$-values where exotic nuclei are produced. As can be seen in Fig. 4, even for higher counting rates the background-to-signal value remains small. The absolute mass calibration was confirmed by observing the yield enhancement of the N=82 ^{132}Sn and ^{134}Te isotopes.

3 Results

The velocity distributions of selected isotopes were used to test the reaction kinematics calculation developed in Ref.

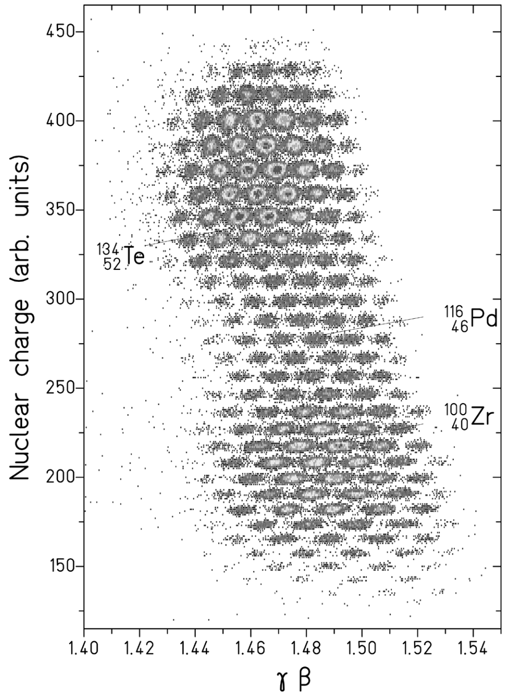

Fig. 4. $Z - \beta\gamma$ scatter-plot of fission fragments observed at $B\rho = 1.04B\rho_0$

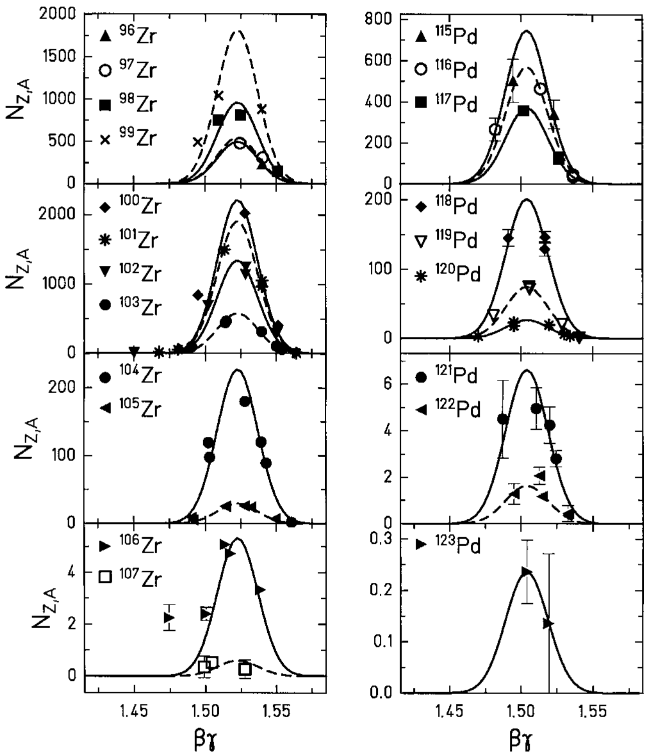

Fig. 5. $\beta\gamma$-distribution for Zr and Pd isotopes in the first stage of the FRS. Each *point* gives the mean $\beta\gamma$ of the events collected in one magnetic setting for a given isotope. The *lines* result from a Gaussian fit

[6]. The FRS transmission being under control, individual cross sections were deduced.

3.1 Determination of the velocity distributions

For forward-emitted fragments, the $\beta\gamma$-distributions were reconstructed for each isotope combining data taken at magnetic settings with $\frac{B\rho}{B\rho_0} > 1$. Figure 5 shows an example for Zr and Pd isotopes. Each point gives the normalized count rate $\mathcal{N}_{Z,A}$ and the mean $\beta\gamma$-value measured in one given setting. The $\mathcal{N}_{Z,A}$-values are normalized to the number of incident U-ions and the number of atoms in the target. They are corrected for the dead time measured by counting the trigger events registered in the scintillator set in the final focal plane and those accepted by the data acquisition. Statistical errors are weighted by a factor which depends on the position of the isotopes in the midplane of the FRS: the mean position at this dispersive focal plane gives indeed an indication of the fraction of the momentum distribution transmitted by the spectrometer.

For a given element the $\beta\gamma$-distributions are found *(i)* to be centered at nearly the same $\beta\gamma$-value and *(ii)* to have the same width $\sigma_{\beta\gamma}$.

i) The independence of the mean velocity in an isotopic series results from fission kinematics. By considering the total kinetic energy equal to the first order to the Coulomb repulsion, the velocity dependence on the mass for a given element can easily be calculated. However, the velocity difference between isotopes is kinematically reduced by a factor $\beta_F/\beta_0 \simeq 18$ in the laboratory frame, β_F being the fragment velocity in the CM-system and β_0 the projectile velocity. The $\beta\gamma$ difference between two Zr isotopes separated by 10 mass units then reaches 5×10^{-3}. The variation of the energy loss between these two fragments in half the target leads to a difference even smaller. Such an accuracy is difficult to achieve with our method.

ii) The observed momentum widths reflect more the target thickness than the fission process. Indeed, the 12 MeV FWHM on average caused by the fission process itself [20] is converted into 0.4 % in the $\beta\gamma$ scale in the laboratory frame. This value of 0.4 % is small compared to the width obtained by the convolution of the 2% momentum acceptance of the spectrometer and of the rectangular function representing the "location straggling". The latter, with a width of 3.3 % for Zr, comes from the energy-loss fluctuations of the U and of the fragments in the target linked to the position where the reaction takes place. Our method is not precise enough to exhibit the small difference of momentum width to be expected for the different Zr-isotopes.

The $\beta\gamma$-distributions of all isotopes of a given element were fitted simultaneously using the conditions *i)* and *ii)*: the centroid, the width (taken identical in an isotopic series) and the maximum yield of each curve $\mathcal{N}^{max}_{Z,A}$ were free parameters. Figure 5 displays the fit result for Zr and Pd isotopes.

Figure 6 shows the mean velocity β_F converted into the center of mass system for each measured atomic number. To transfer β-values of forward emitted fragments from

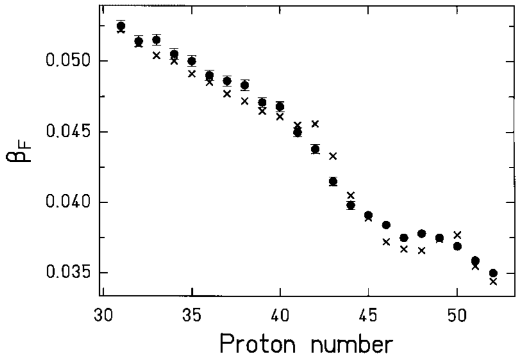

Fig. 6. Mean β-values in the center of mass versus proton number. *Full points* come from fit calculations described in the text, *crosses* result from a compilation for ^{235}U(n_{th},f) [20–22]

the laboratory frame to the center of mass system, the energy losses of the most probable mass for each element in the intermediate focal plane plastic detector and in the target were considered. The β_F-values were compared to those obtained in thermal neutron-induced fission of ^{235}U [20–22]. The observed agreement justifies the use of the velocities measured for ^{235}U(n_{th},f) in the calculation of the transmission of the fragments through the spectrometer. Moreover, the contribution of the "location straggling" to the momentum width, extracted from the fit results for each element, is in perfect agreement with the expected values [16].

3.2 Determination of the isotopic cross sections

Isotopic cross sections for fragments located between Ga and Te were deduced from $\beta\gamma$-distributions. They were calculated from:

$$\sigma(Z,A) = \sum_{\beta\gamma} \mathcal{N}_{Z,A}(\beta\gamma)/T_{\Omega}(Z) \qquad (1)$$

where T_{Ω} is the angular transmission determined from the transmission values $T_{max}(Z)$ along the central trajectory calculated by the MOCADI code. $T_{max}(Z) = T_{\Omega}(Z) * T_P$ with $T_P = \frac{0.02 B\rho}{2.35\sigma_{\beta\gamma}}$ being the momentum transmission. For a Gaussian distribution, it involves:

$$\sigma(Z,A) = 1.07 \mathcal{N}_{Z,A}^{max}/T_{max}(Z) \qquad (2)$$

The given uncertainties (FWHM) concern only uncertainties on $\mathcal{N}_{Z,A}^{max}$. Indeed, in previous experiments, the efficiency of the MUSIC and of the plastic detectors were measured to be close to 100%. The beam absorption in half the target reaches 2% and secondary reactions of fission fragments with the target, and even more in the scintillators, are negligible. These corrections were finally not taken into account in our evaluation of the uncertainties. The evaluation of the transmission value and the measurement of the beam intensity lead to a systematic error around ±20%.

Isotopic cross sections are depicted in Fig. 7 for the elements between Ga and Te and for magnetic settings with $\frac{B\rho}{B\rho_0} > 1$. Only cross sections with uncertainties smaller than 50% are considered. For the first time, yields of all isotopes were determined consistently in a short beam time, without dependence on β-decay half lives or radiochemical efficiencies. Many short-lived fragments heavier than Pd are clearly identified as fission fragments for the first time. These data bring a decisive piece of information to unify the previous descriptions of fission in the low excitation energy domain.

4 Extraction of the low-energy fission component

4.1 Conclusions drawn from elemental yields

The elemental yields of the low-energy fission component were already analysed for Pb and Be targets [6]. The yields related to events coming from a weakly excited fissioning nucleus were determined according to the Bρ distribution of each element. Figure 8a presents the Z-distribution of the light fission fragments measured with a Pb target compared to results obtained for thermal neutron-induced fission of ^{235}U. The Z-distribution measured with a Be target is displayed in Fig. 8b. The observed peak-to-valley ratio of 2.2 suggests a mean excitation energy of 25 MeV for the Be target. Using the data measured for the U/Be-system as a standard for nuclear fission, the Z-distribution related to electromagnetic dissociation for the U/Pb-system was obtained by substracting the Z-yields measured with the U/Be-system scaled by a factor of 2.3 [28] to the yields measured with the Pb target. The electromagnetic and nuclear contributions are presented separately in Fig. 8c. The resulting cross section for the electromagnetic fission processes is 1.9±0.2 b. The contribution of the nuclear processes is evaluated to 10% for asymmetric fission events (from Se to Zr), 25% for symmetric fission events and 17%, 20% and 30% for As, Ge and Ga very asymmetric fission elements, respectively. A total cross section for nuclear low-energy fission of 0.26±0.09 b is obtained.

The Z-distribution related to electromagnetic processes is characterized by a peak-to-valley ratio of 7.1±1.0 and a proton odd-even effect in the peaks of 8.6 %. A mean excitation energy of about 9 MeV in ^{238}U was deduced from odd-even effects in the peaks. In the valley the measured peak-to-valley ratio suggests rather an excitation energy around 19 MeV. If the low energy can be safely related to the GDR resonance, the 19 MeV could be linked to the two-phonon GDR. The differential cross sections for the GDR, GQR and two-phonon GDR (DGDR) were calculated [29] as a function of the virtual photon energy for the U/Pb system from a theoretical investigation of Bertulani and Baur [30] (see Fig. 9). The photoabsorption cross sections were normalized to the cross sections published by Caldwell [31] and the impact parameter cut-off was chosen according to [28]. Such a cross

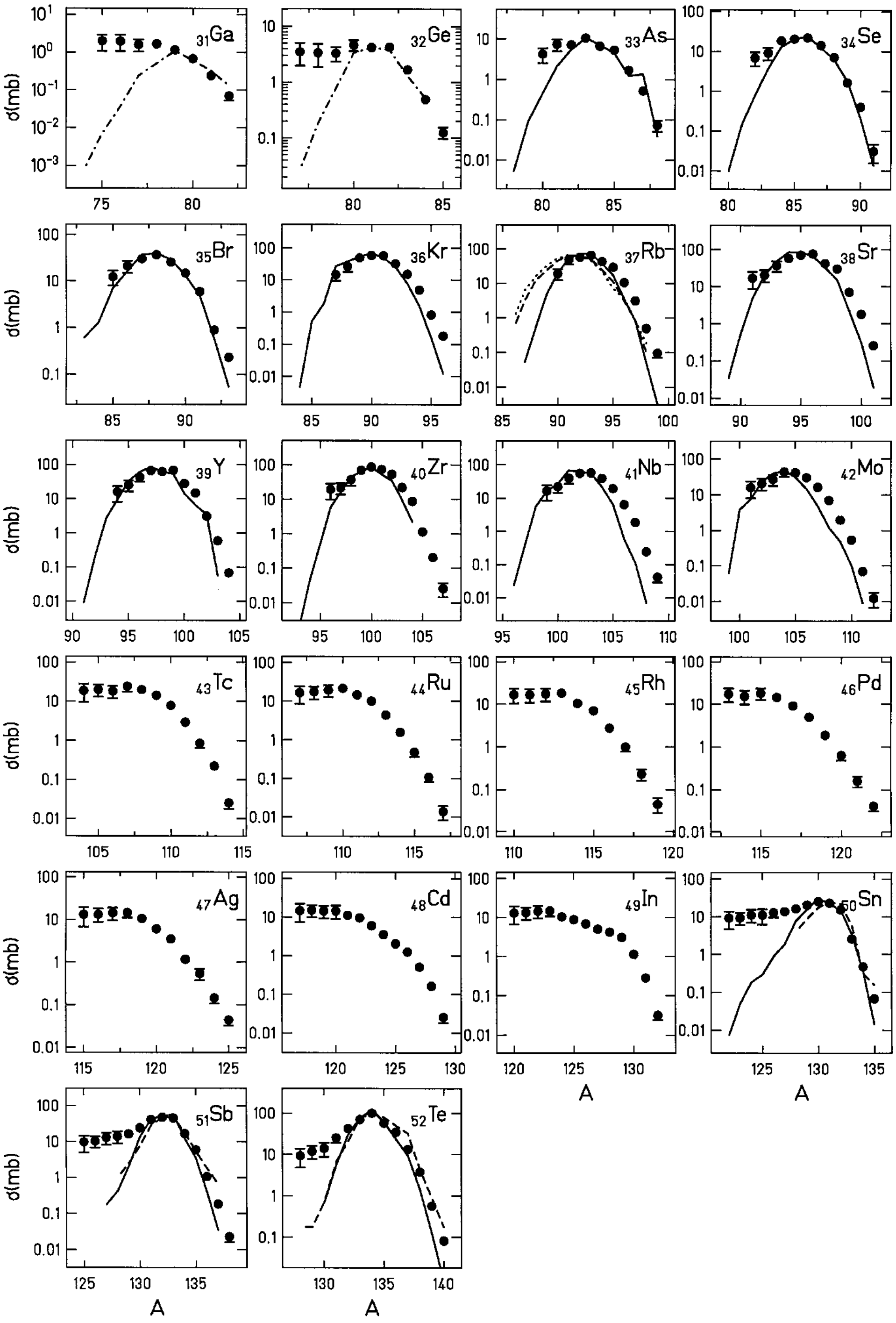

Fig. 7. Production cross sections measured for isotopes with magnetic rigidities $\frac{B\rho}{B\rho_0} > 1$ (*full points*) compared with results found in literature. *Full lines* indicated for Z=33-42 and Z=50-52 come from the recommended independent yields based on the Z_P model for ^{235}U(n$_{th}$,f) [23]. The *dashed-dotted lines* for Z=31-32 are measured data for ^{235}U(n$_{th}$,f) [21]. For Rb isotopes results of proton-induced fission of ^{238}U are shown for 40 MeV (*dashed line*) and 60 MeV (*dotted line*) proton energy [24]. ^{238}U(γ,f) with 11 MeV endpoint energy are displayed for Sn, Sb and Te (*dashed line*) [25]. For a clearer presentation, each curve was normalized to the maximum value of the *full points* linked to low-energy fission

section spectrum must be convoluted by the fission probability. Whereas first-chance fission dominates around 12 MeV excitation energy, the region around 20-30 MeV leads to higher-chance fissions; the mean mass of the fissioning Uranium is shifted to 237 [29,32]. At the same time, the excitation energy available for the fission process itself is shifted towards smaller values. Finally, the calculated electromagnetic fission cross section is 1.66 b. It is shared among 95 mb for IS-GQR, 85 mb for IV-GQR, 1227 mb for GDR and 256 mb for DGDR. However, these relative contributions change according to the fission fragment mass. It was estimated that the DGDR resonance is responsible for 50% of the EM symmetric fission events [6].

4.2 Analysis of the measured isotopic distributions

The analysis of the isotopic distributions provides the access to one of the major characteristics of low-energy fission. However, the kinematical condition $\frac{B\rho}{B\rho_0} > 1$ alone

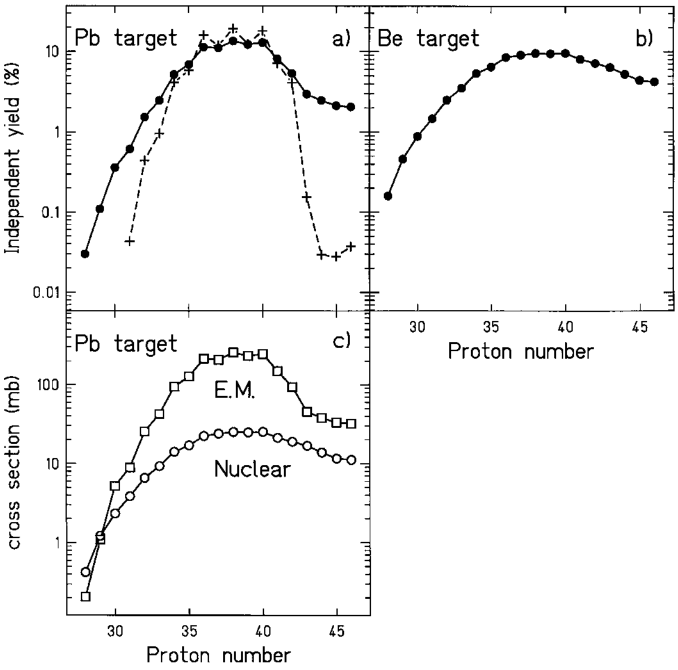

Fig. 8. **a** Elemental fission yields measured with the Pb target (*full points*) compared to the results obtained in thermal neutron-induced fission of ^{235}U [23] (*crosses*). **b** Elemental fission yields measured with the Be target. For both targets, the yields are normalized on the light branch of fission [6]. **c** Elemental cross sections established for the electromagnetic (*squares*) and nuclear (*points*) contributions for the U/Pb-system

was not constraining enough to select low-energy fission events. A detailed analysis of the production rates was required to derive isotopic cross sections of the low-energy fission process.

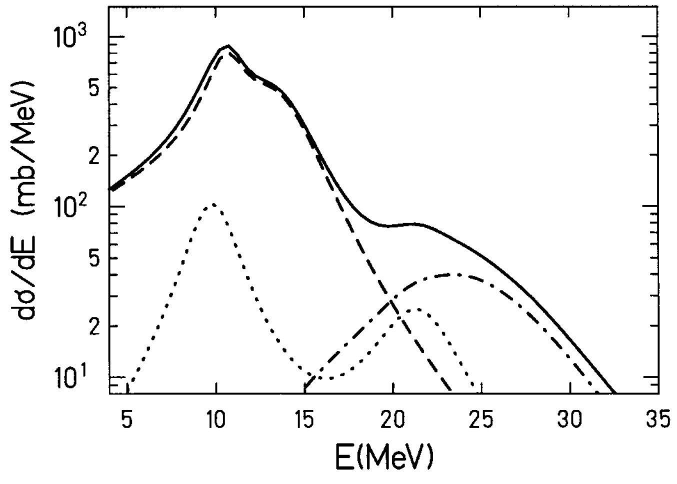

Fig. 9. Electromagnetic differential fission cross section (*full line*) calculated as a function of the virtual photon energy for 750 AMeV U on Pb. The GDR (*dashed-line*), GQR (*dotted line*) and DGDR (*dashed-dotted line*) contributions are separately displayed [29]

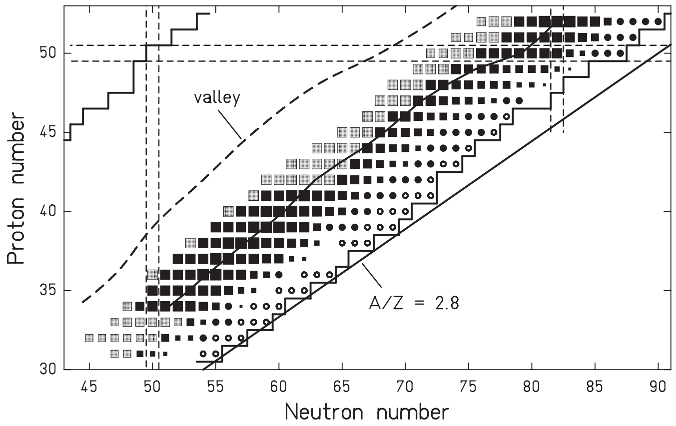

Fig. 10. Section of the chart of nuclei presenting an overview of the measured fission isotopes with cross sections lying between 10 μb and 100 mb. Only fragments with $\frac{B\rho}{B\rho_0} > 1$ are displayed. *Black squares* symbolise fragments coming from the low-energy fission component. *Grey squares* correspond to isotopes coming from a mixture with higher-energy fission processes. The *full line* shows the ridge of isotopes linked to low-energy fission. Isotopes indicated by a *full circle* were found in special settings optimized to search new isotopes [5]. The *open circles* correspond to isotopes measured with the same method but with a larger rate of incident ^{238}U-ions per second and a Be target [26,27]

Figure 10 shows the location of the detected fragments and of the new identified neutron-rich isotopes on the chart of nuclei. It gives a first insight into the N/Z ratio of the fragments selected by $\frac{B\rho}{B\rho_0} > 1$: they are all located on the neutron-rich side of the β-stability valley. Most of them are even more neutron-rich than the most abundant fission products found in thermal neutron-induced fission of ^{235}U. In this Fig., the isotopes exclusively produced in a low-energy fission process are indicated with full black squares with the associated ridge. This line is less than one neutron apart from the ridge of isotopes produced in ^{235}U(n$_{th}$,f). The corresponding A/Z-values are approximatively comprised in the interval [2.6,2.8]. Events with magnetic rigidities $\frac{B\rho}{B\rho_0} < 1$ (not represented here) continuously populate less neutron-rich nuclei. These fragments produced in higher-energy fission [33] and in fragmentation [34] will be discussed in other forthcoming papers.

The shape of the mass distributions displayed in Fig. 7 varies significantly from one element to another. Whereas the shape is approximatively Gaussian for Se to Mo (elements which populate the light peak of asymmetric fission), an over-production of isotopes with lower A/Z-values is found for the other elements. These isotopic yields, which amount to about 10-20 mb, come from a tail from higher excitation energy fissions. They are represented by grey squares in Fig. 10.

In the following, the most probable mass value A_P for each element is used to estimate the excitation energy of the fissioning U isotope. For this purpose, the evolution of the mean post-scission neutron number $\bar{\nu}(A)$ with the excitation energy of the fissioning nucleus has to be known.

Table 1. Most probable mass value A_P deduced from Gaussian fits of measured isotopic distributions. $A_P[12MeV]$ are calculated from the relation (3) with 12 MeV excitation energy

Z	34	35	36	37	38	39	40	52
A_P	85.3(1)	87.9(1)	90.3(1)	92.8(1)	95.3(1)	97.9(1)	100.4(1)	133.9(1)
$A_P[12.MeV]$	86.3	88.5	90.7	93.0	95.4	97.7	100.0	134.3

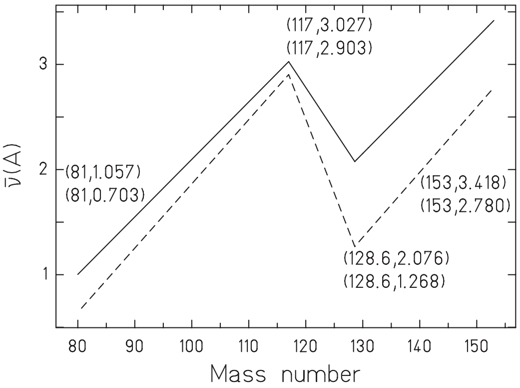

Fig. 11. Mean number of emitted post-scission neutrons versus fragment mass parametrized for an excitation energy in the fissioning nucleus of 12 MeV (*dashed line*) and 20 MeV (*full line*)

The saw tooth structure $\bar{\nu}(A)$ was measured for about 12 MeV [35–38] and 21 MeV [35,36] proton-induced fission of ^{238}U. The fissioning nucleus is not the same as in our case, but the very close values for the neutron binding energies in ^{239}Np and ^{238}U justify the use of these experimental data. Two curves describing the gross features of the $\bar{\nu}$-values as function of the mass split were parametrized [39]. The $\bar{\nu}(A)$-values related to a fissioning nucleus sustaining 12 and 20 MeV excitation energy were interpolated from this parametrization (see Fig. 11) with an estimated uncertainty of ±0.2 neutron. The uncertainty may be higher in the mass domain A=125-135 where the number of evaporated neutrons is highly sensitive to the damping of the shell effects with excitation energy around ^{132}Sn. Note that this parametrization links the post-scission neutron number to the energy released in the system before pre-fission neutron evaporation. The mean masses of the U isotopes after pre-fission neutron evaporation, called A_0, were taken as 237.8 at 12 MeV and 237.2 at 20 MeV excitation energy with an uncertainty of ±0.2 amu.

Elements were gathered according to the behaviour of their isotopic distribution:

i) The distributions from Se to Zr and of Te were fitted by a Gaussian curve. The measured A_P-values were compared to the expected most probable masses, assuming a mean excitation energy linked to the GDR resonance centered at 12 MeV (see Table 1). These values were computed from the following relation:

$$A_P(Z) = {A'_P}^{(^{236}U)}(Z)\frac{A_0}{236} - \bar{\nu}(A_P) \qquad (3)$$

with ${A'_P}^{(^{236}U)}(Z)$ being the mean mass before the evaporation of post-scission neutrons evaluated from the A'_P-model proposed by Wahl for thermal neutron-induced fission of ^{235}U [23]. The good agreement obtained (see Table 1) shows that the electromagnetic contribution around the GDR resonance is indeed well separated from higher-energy fission processes for the five elements populating the top of the light fission peak.

ii) The discrepancy observed in A_P-values when Z decreases below 36 illustrates that the GDR excitation cannot be disentangled from processes with higher excitation energies. The situation becomes worse for elements lighter than Se since the distributions lose their Gaussian shape.

iii) The shape of the isotopic distributions in the valley is similar to the one measured for very asymmetric fission events: the Gaussian neutron-rich component cannot be easily extracted.

iiii) The Sn, Sb and Te distributions can be fitted by a Gaussian curve at least for the neutron-rich part. The high energy contribution is better transmitted in these elements than in their respective light partners Mo, Nb, Zr.

4.3 Construction of the isotopic distributions linked to low-energy fission

The previous overview shows that, except for elements Se to Zr, the low-energy fission component cannot be directly deduced from Fig. 7: the centroids of the distributions are not easy to delineate. However, the shape of these distributions, e.g. for In, encourage to pursue the analysis. Based on previous knowledge, reasonable assumptions helped to obtain realistic isotopic distributions exclusively linked to the low-energy fission component. The symmetrical image of the neutron-rich side of the distributions was constructed for

a) elements mentioned in point *i)* where this component is well isolated

b) elements regrouped in points *iii)* and *iiii)* for which the pairs of complementary partners (Z) and (92-Z) were measured.

a) The reconstruction of the isotopic distributions for elements from Se to Zr is illustrated at the top of Fig. 12 for the Sr element. The primary distribution, before neutron evaporation, (Fig. 12-1b) was deduced from the measured one (Fig. 12-1a) by means of $A' = A + \bar{\nu}(A)$, $\bar{\nu}(A)$ being computed with 12 MeV excitation energy. The mirror of this figure was constructed symmetrically with respect to the fitted most probable value A'_P leading to Fig. 12-1c. The full symbols represent the shifted measured val-

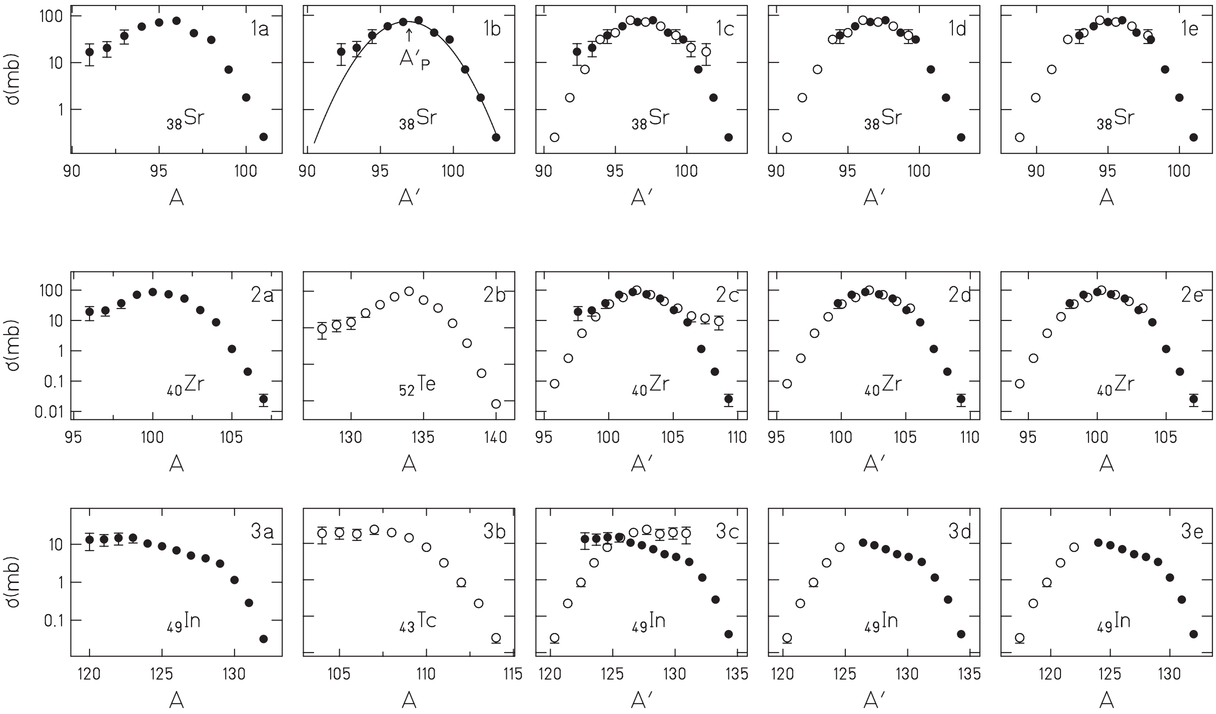

Fig. 12. *First line:* Reconstruction steps of the low-energy fission isotopic distributions for Sr. **1a** measured distribution, **1b** deduced primary distribution with the associated fit, **1c** primary distribution (*full points*) and its mirror image (*open points*), **1d** same as **1c** without the higher-energy fission points, **1e** reconstructed secondary distribution. *Second line:* Reconstruction steps of the low-energy fission isotopic distributions for Zr : **2a** Zr measured distribution, **2b** charge partner Te measured distribution, **2c** Zr primary distribution constructed from Zr measured distribution (*full points*) and from Te measured distribution (*open points*), **2d** same as **2c** without the higher-energy fission points, **2e** Zr reconstructed secondary distribution. *Third line:* same as the second line for the In/Tc pair

ues, the open symbols the mirror values. The two points at the extremity of each curve with large yields are understood as a mixture of the GDR component with higher-energy fission processes. These points were suppressed in Fig. 12-1d. The secondary isotopic distribution (after neutron evaporation) was finally deduced (see Fig. 12-1e).

b) The Zr/Te pair was chosen in Fig. 12 to illustrate the procedure used to construct the low-energy fission distributions of elements Zr to Te. Whereas the neutron-rich Zr isotopes are produced only by the low-energy component, the neutron-deficient part is mixed with higher-energy processes (Fig. 12-2a). In a low-energy fission event a neutron-deficient Zr isotope is accompanied by a neutron-rich Te isotope (Fig. 12-2b). The primary low-energy fission distribution of Zr isotopes (Fig. 12-2c) was constructed by means of the primary production of Zr isotopes for the neutron-rich side and by the primary production of Te isotopes for the neutron-deficient side using $A'_{Zr} = A_0 - A'_{Te}$. In Fig. 12-2c the full points represent the Zr-values, the open points the reconstructed values from the Te distribution. These points are shifted in mass according to the $\bar{\nu}(A)$ and A_0-values corresponding to the excitation energy deposited in the U isotope. The 12 MeV of the GDR was used for the elements Sn, Sb and Te and their partner. For elements between Tc to In, that means for symmetric fission events, the observed peak-to-valley ratio demands to choose rather 20 MeV excitation energy. The point where to change between these two excitation energy domains is rather arbitrary, but the poor knowledge on the neutron evaporation for a given isotope at a fixed excitation energy value does not justify a more sophisticated procedure. In Fig. 12-2d the points coming from a mixture with higher-energy fission processes were suppressed. Figure 12-2e displays the secondary isotopic distribution of Zr after post-scission neutron evaporation related to low-energy fission.

The same construction is shown for the In isotopic distributions in the last line of Fig. 12. The secondary isotopic distributions for low-energy fission are displayed in Fig. 13 from elements Se to Te. The good agreement observed in absolute cross sections between the two independently measured distributions of Zr and Te confirms that the process is dominated by the GDR excitation. This remains true for the Sb/Nb pair. The Sn and Mo distributions cannot be perfectly superimposed: the cross sections of Sn in the mass range 126-130 were used in the analysis in order to eliminate a possible mixture of processes. The distributions from Nb to Ru show clearly the contribution of two components. Fits were performed according to this hypothesis. For elements from Mo to Pd, the open points are shifted according to the assumed excitation energy of the U isotope. The parameters of the Gaussian

Table 2. Fit parameters for primary isotopic distributions: elemental yields $Y(Z)$, most probable mass values A'_P and mass dispersions σ'_A. Left part: asymmetric fission modes. Right part: symmetric fission mode. A'_P(Z)=237.2-$A'_P(92-Z)$ for Z=47-49, A'_P(Z)=237.8-$A'_P(92-Z)$ for Z=50-52

Z	Y(Z) (%)	A'_P	σ'_A	Y(Z) (%)	A'_P	σ'_A
34	4.0 ± 0.2	86.4 ± 0.1	1.67 ± 0.05			
35	6.0 ± 0.3	89.0 ± 0.1	1.65 ± 0.03			
36	11.1 ± 0.6	91.4 ± 0.1	1.76 ± 0.03			
37	11.4 ± 0.7	94.1 ± 0.1	1.86 ± 0.04			
38	13.8 ± 0.8	96.8 ± 0.1	1.84 ± 0.04			
39	13.1 ± 0.6	99.5 ± 0.1	1.78 ± 0.03			
40	15.4 ± 0.7	102.2 ± 0.1	1.71 ± 0.03			
41	8.2 ± 0.6	104.3 ± 0.1	1.55 ± 0.04	1.1 ± 0.6	107.0 ± 0.4	1.23 ± 0.12
42	3.4 ± 0.4	106.2 ± 0.2	1.43 ± 0.05	1.6 ± 0.4	108.9 ± 0.4	1.46 ± 0.10
43	0.5 ± 0.1	107.0 ± 0.2	1.36 ± 0.08	1.9 ± 0.1	111.0 ± 0.1	1.69 ± 0.06
44	0.11 ± 0.06	109.5 ± 0.6	1.27 ± 0.18	2.0 ± 0.1	113.6 ± 0.1	1.74 ± 0.06
45	0.01 ± 0.02	111.8 ± 1.2	1.32 ± 0.05	2.0 ± 0.1	116.2 ± 0.1	1.70 ± 0.05
46				2.3 ± 0.1	118.6 ± 0.1	1.72 ± 0.03

Table 3. Fit parameters for secondary isotopic distributions: elemental yields $Y(Z)$, most probable mass values A_P and mass dispersions σ_A. Left part: asymmetric fission modes. Right part: symmetric fission mode. The $Y(Z)$ values should be symmetric around Z=46: the small observed discrepancies show the limit of accuracy of our method

Z	Y(Z) (%)	A_P	σ_A	Y(Z) (%)	A_P	σ_A
34	4.2 ± 0.2	85.3 ± 0.1	1.61 ± 0.04			
35	6.2 ± 0.3	87.9 ± 0.1	1.53 ± 0.04			
36	11.1 ± 0.6	90.3 ± 0.1	1.62 ± 0.04			
37	11.3 ± 0.8	92.8 ± 0.1	1.69 ± 0.05			
38	14.3 ± 0.8	95.3 ± 0.1	1.72 ± 0.05			
39	12.9 ± 0.8	97.9 ± 0.1	1.66 ± 0.04			
40	14.5 ± 0.2	100.4 ± 0.1	1.60 ± 0.01			
41	8.2 ± 0.6	102.3 ± 0.1	1.44 ± 0.04	1.3 ± 0.6	104.8 ± 0.4	1.18 ± 0.11
42	3.5 ± 0.4	104.1 ± 0.1	1.35 ± 0.05	1.6 ± 0.5	106.6 ± 0.3	1.38 ± 0.09
43	0.5 ± 0.1	104.7 ± 0.2	1.26 ± 0.07	2.0 ± 0.1	108.5 ± 0.1	1.60 ± 0.06
44	0.1 ± 0.1	107.0 ± 0.5	1.20 ± 0.18	1.9 ± 0.1	110.8 ± 0.1	1.68 ± 0.06
45	0.008 ± 0.015	108.8 ± 1.5	1.23 ± 0.01	2.0 ± 0.1	113.3 ± 0.1	1.65 ± 0.05
46				2.4 ± 0.1	115.8 ± 0.1	1.71 ± 0.03
47	0.03 ± 0.03	122.5 ± 0.6	1.32 ± 0.01	2.3 ± 0.1	118.2 ± 0.1	1.72 ± 0.05
48	0.2 ± 0.1	125.4 ± 0.5	1.35 ± 0.17	2.2 ± 0.1	121.0 ± 0.1	1.86 ± 0.06
49	0.5 ± 0.1	128.0 ± 0.2	1.30 ± 0.07	2.3 ± 0.2	123.8 ± 0.1	1.84 ± 0.06
50	3.0 ± 0.5	130.3 ± 0.2	1.32 ± 0.05	2.5 ± 0.6	127.7 ± 0.4	1.76 ± 0.11
51	8.0 ± 0.7	132.0 ± 0.1	1.45 ± 0.04	1.5 ± 0.7	129.6 ± 0.6	1.44 ± 0.16
52	14.3 ± 0.2	133.9 ± 0.1	1.61 ± 0.01			

distributions depend on this assumption. They are given in Table 2 for primary distributions and in Table 3 for secondary distributions. The elemental yields calculated from $Y(Z) = \sum_A Y(Z,A)$ and given in Table 3 are close (absolute discrepancy of less than 1.6%) to the values presented in Fig. 8a. The fractional independent yields $\frac{Y(Z,A)}{Y(Z)}$ linked to the low-energy fission component can easily be computed (see Table 4). A total cross section of 2.2±0.2 b is found. It is consistent with the 2.1±0.2 b deduced from Z-measurement [6].

From parameters given in Table 3 isobaric distributions were fitted from A=85 to A=134. Results are given in Table 5. To first order a Gaussian fit was used for each distribution. The small deviations induced by the presence of two Gaussian distributions for elements between Nb and Sb were found smaller than the given errors.

4.4 Interpretation of the low-energy fission isotopic distributions in terms of fission modes

According to the static scission-point model of Wilkins et al [11] the isotopic yields depend on the competition between several modes caused by important shell corrections. Following this model, isotopes populating the fission peaks are produced in scission configurations dominated by the strong deformed neutron shell around N=88 and

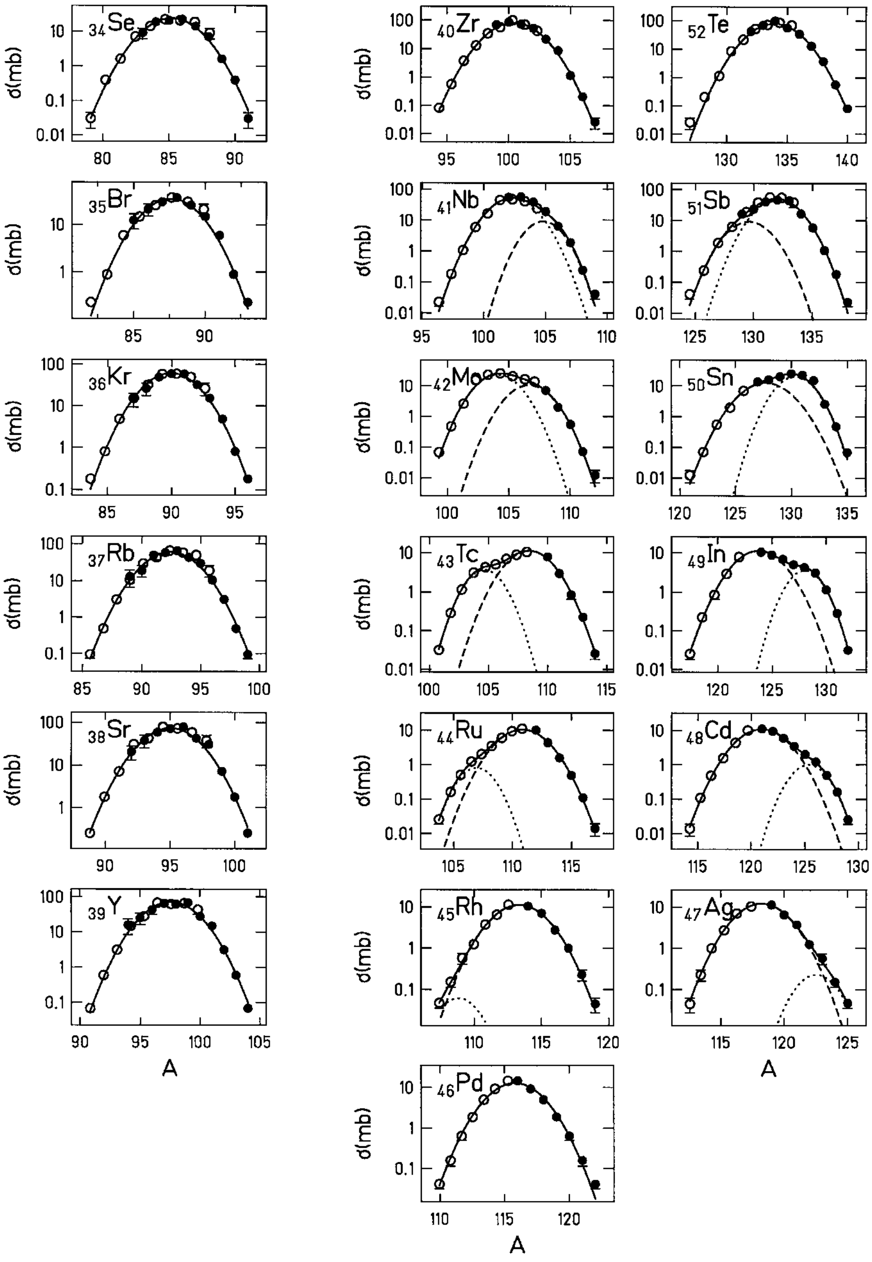

Fig. 13. Secondary isotopic distributions of low-energy fission from elements Se to Te and the associated fits

the spherical closed shell N=82. In the Brosa terminology [12], these two configurations are correlated to the "Standard II" and "Standard I" channels, respectively. They will be called "asymmetric modes" here. A third mode, linked to extremely deformed scission configurations, accounts for the production of symmetric fragmentations. This "Super-long" channel correlates to liquid drop fission in the potential energy calculation. The increase of this "symmetric mode" with the excitation energy deposited in the entrance channel is well known for the $Y(A)$-distributions. It is only little studied in the isotopic distributions.

Figure 13 shows that the isotopic distribution of light elements in the asymmetric fission peak (Se to Zr) is nicely reproduced by a single Gaussian distribution. However, the measured In and Tc distributions displayed in Fig. 13 are not symmetric; the secondary In distribution presents a bump around A=129. This double structure was already investigated by Rudstam et al [40] and discussed by Wahl for thermal neutron-induced fission of ^{235}U [41]. It is interpreted as a support of the old "two-modes-of-fission hypothesis" proposed by Turkevich and Niday [10]. Figure 13 presents a fit using two Gaussian curves to describe the In and Tc distributions. Each curve is correlated to a well-defined scission configuration. The more neutron-rich component of the In distribution is assumed to come from an asymmetric scission configuration with a heavy nearly spherical fragment in the vicinity of the N=82 shell. The more neutron-deficient component would come from an elongated configuration with two fragments

Table 4. Fractional independent yields $\frac{Y(A,Z)}{Y(Z)}$ of the low-energy fission component for elements Se to Te. Isotopes marked with a * are the new identified nuclei

Z	A	$\frac{Y(A,Z)}{Y(Z)}$	Z	A	$\frac{Y(A,Z)}{Y(Z)}$
34	82	2.98 ± 0.43	38	91	1.04 ± 0.26
	83	8.84 ± 0.84		92	3.73 ± 0.64
	84	17.80 ± 1.11		93	9.55 ± 1.12
	85	24.35 ± 1.16		94	17.46 ± 1.40
	86	22.63 ± 1.16		95	22.81 ± 1.44
	87	14.28 ± 1.04		96	21.28 ± 1.44
	88	6.12 ± 0.69		97	14.18 ± 1.32
	89	1.78 ± 0.30		98	6.75 ± 0.93
	* 90	0.35 ± 0.09		99	2.30 ± 0.46
	* 91	0.05 ± 0.02		100	0.56 ± 0.16
35	85	4.52 ± 0.67		101	0.10 ± 0.04
	86	12.38 ± 1.18	39	94	1.54 ± 0.33
	87	22.16 ± 1.42		95	5.28 ± 0.80
	88	25.93 ± 1.44		96	12.60 ± 1.30
	89	19.82 ± 1.39		97	20.87 ± 1.52
	90	9.90 ± 1.06		98	24.02 ± 1.52
	91	3.23 ± 0.54		99	19.21 ± 1.50
	92	0.69 ± 0.17		100	10.67 ± 1.20
	93	0.10 ± 0.03		101	4.12 ± 0.68
36	87	3.22 ± 0.56		102	1.10 ± 0.26
	88	9.24 ± 1.08		* 103	0.21 ± 0.07
	89	18.13 ± 1.43		* 104	0.03 ± 0.01
	90	24.29 ± 1.49		* 105	0.002 ± 0.001
	91	22.24 ± 1.49	40	96	0.57 ± 0.02
	92	13.91 ± 1.31		97	2.59 ± 0.08
	93	5.94 ± 0.84		98	8.05 ± 0.17
	94	1.73 ± 0.36		99	16.91 ± 0.29
	95	0.35 ± 0.10		100	24.09 ± 0.39
	* 96	0.05 ± 0.02		101	23.25 ± 0.37
37	90	5.88 ± 1.00		102	15.21 ± 0.27
	91	13.22 ± 1.53		103	6.74 ± 0.15
	92	20.97 ± 1.73		104	2.02 ± 0.06
	93	23.45 ± 1.73		105	0.41 ± 0.02
	94	18.49 ± 1.70		* 106	0.057 ± 0.003
	95	10.28 ± 1.37		* 107	0.0053 ± 0.0004
	96	4.03 ± 0.78			
	97	1.11 ± 0.31			
	98	0.22 ± 0.08			
	99	0.03 ± 0.02			

Table 4. Continued

Z	A	$\frac{Y(A,Z)}{Y(Z)}$	Z	A	$\frac{Y(A,Z)}{Y(Z)}$
41	99	1.84 ± 0.44	44	107	3.39 ± 1.07
	100	6.96 ± 1.13		108	6.57 ± 1.14
	101	16.30 ± 1.78		109	12.72 ± 1.29
	102	23.83 ± 1.97		110	19.89 ± 1.50
	103	22.51 ± 2.18		111	22.41 ± 1.58
	104	15.28 ± 2.47		112	17.76 ± 1.43
	105	8.43 ± 2.33		113	9.88 ± 1.11
	106	3.51 ± 1.61		114	3.86 ± 0.66
	107	0.89 ± 0.66		115	1.06 ± 0.27
	* 108	0.12 ± 0.14		* 116	0.20 ± 0.07
	* 109	0.008 ± 0.013		* 117	0.03 ± 0.01
	* 110	0.0003 ± 0.0006		* 118	0.003 ± 0.002
42	101	1.51 ± 0.50	45	110	3.21 ± 0.45
	102	6.25 ± 1.40		111	8.86 ± 0.75
	103	15.05 ± 2.31		112	17.33 ± 1.11
	104	21.70 ± 2.75		113	23.55 ± 1.45
	105	20.50 ± 3.03		114	22.19 ± 1.37
	106	15.49 ± 3.02		115	14.50 ± 0.98
	107	10.73 ± 2.74		116	6.57 ± 0.64
	108	5.89 ± 2.13		117	2.06 ± 0.32
	109	2.12 ± 1.12		* 118	0.45 ± 0.11
	110	0.47 ± 0.35		* 119	0.07 ± 0.02
	* 111	0.06 ± 0.06		* 120	0.007 ± 0.003
	* 112	0.005 ± 0.007		* 121	0.0005 ± 0.0003
	* 113	0.0002 ± 0.0004	46	113	6.14 ± 0.44
43	104	6.07 ± 1.11		114	13.43 ± 0.78
	105	8.20 ± 1.23		115	20.88 ± 1.11
	106	9.81 ± 1.30		116	23.11 ± 1.22
	107	14.26 ± 1.43		117	18.20 ± 0.99
	108	19.22 ± 1.56		118	10.20 ± 0.63
	109	18.72 ± 1.55		119	4.07 ± 0.33
	110	12.44 ± 1.34		120	1.15 ± 0.13
	111	5.60 ± 0.89		* 121	0.23 ± 0.04
	112	1.70 ± 0.41		* 122	0.03 ± 0.01
	113	0.35 ± 0.12		* 123	0.003 ± 0.001
	* 114	0.05± 0.02			
	* 115	0.005± 0.003			

of close masses. For Indium, located in the transition region between the valley and the heavy peak, the yields of the symmetric fission mode are larger than those of the asymmetric fission mode. The situation was just opposite for thermal neutron-induced fission of ^{235}U. The enhancement of the mode of symmetric fission in our case is undoubtedly related to the larger excitation energies in the entrance channel. A similar behaviour is shown for the Cd and Ru pair. The large strength of the symmetric fission mode is seen in the Sn and Sb distributions, and their partner, as well. The reconstructed Ag distribution shows still a light asymmetry towards the neutron-rich side evaluated to a few percent, whereas the Pd distribution is well fitted by a unique Gaussian related to the symmetric scission configuration.

The measured cross sections of the most probable mass values of the Zr and Te distributions are similar (see Fig. 13). This allows to deduce a mean number of total post-scission neutrons $\bar{\nu}_{tot}$ without making any hypothesis on the excitation energy of the fissioning U isotope. From $A_0 - (A_{P(Zr)} - A_{P(Te)})$, we obtain $\bar{\nu}_{tot}$=3.5 for this pair. $\bar{\nu}_{tot}$ reaches 5.6 neutrons for the Pd isotopes. For each measured pair, $\bar{\nu}_{tot}$ was deduced from the most probable masses linked to each mode (see Fig. 14a). This value $\bar{\nu}_{tot}$ is strongly affected by the chosen value of the excitation energy in the entrance channel except for the Zr/Te and Nb/Sb pair. No significant difference of $\bar{\nu}_{tot}$ is observed between the modes. Compared to thermal neutron-induced fission, a shift towards larger values is found: 2.3 and 4 neutrons were observed for the Zr/Te and Pd/Pd pairs in ^{235}U(n$_{th}$,f), respectively .

In the frame of the static scission-point model of Wilkins et al, the energy available for neutron emission is understood as the difference in deformation energy E_{def}

Table 4. Continued

Z	A	$\frac{Y(A,Z)}{Y(Z)}$	Z	A	$\frac{Y(A,Z)}{Y(Z)}$
	115	3.99 ± 0.50		126	6.35 ± 2.07
	116	9.97 ± 0.84		127	10.02 ± 2.48
	117	17.78 ± 1.18		128	13.50 ± 2.71
	118	22.64 ± 1.40		129	17.75 ± 3.14
	119	20.59 ± 1.30	50	130	20.53 ± 3.44
	120	13.43 ± 0.99		131	16.54 ± 2.97
47	121	6.41 ± 0.68		132	8.12 ± 1.81
	122	2.45 ± 0.45		133	2.31 ± 0.71
	123	0.89 ± 0.33		134	0.38 ± 0.17
	124	0.32 ± 0.21		* 135	0.03 ± 0.02
	* 125	0.086 ± 0.085		* 136	0.0019 ± 0.0015
	* 126	0.015 ± 0.019		* 137	0.0001 ± 0.0001
	117	2.05 ± 0.40		125	0.03 ± 0.05
	118	5.60 ± 0.76		126	0.19 ± 0.24
	119	11.45 ± 1.09		127	0.91 ± 0.77
	120	17.53 ± 1.31		128	2.83 ± 1.50
	121	20.11 ± 1.38		129	6.56 ± 2.00
	122	17.34 ± 1.30		130	12.78 ± 2.35
48	123	11.50 ± 1.12		131	20.62 ± 2.50
	124	6.47 ± 0.97	51	132	24.26 ± 2.25
	125	3.73 ± 0.89		133	18.91 ± 1.98
	126	2.18 ± 0.79		134	9.37 ± 1.39
	127	0.99 ± 0.55		135	2.91 ± 0.63
	128	0.29 ± 0.25		136	0.56 ± 0.17
	129	0.05 ± 0.07		*137	0.07 ± 0.03
	120	2.16 ± 0.45		*138	0.005 ± 0.003
	121	5.68 ± 0.82		*139	0.0002 ± 0.0002
	122	11.12 ± 1.14		128	0.028 ± 0.002
	123	16.20 ± 1.31		129	0.22 ± 0.01
	124	17.61 ± 1.35		130	1.24 ± 0.05
	125	14.54 ± 1.27		131	4.68 ± 0.12
49	126	10.16 ± 1.14		132	11.98 ± 0.23
	127	7.90 ± 1.10		133	20.88 ± 0.35
	128	6.89 ± 1.07	52	134	24.75 ± 0.40
	129	4.61 ± 0.91		135	19.95 ± 0.33
	130	1.88 ± 0.55		136	10.94 ± 0.22
	131	0.44 ± 0.20		137	4.08 ± 0.11
	132	0.06 ± 0.04		138	1.04 ± 0.04
	122	0.05 ± 0.05		* 139	0.18 ± 0.01
	123	0.27 ± 0.21		* 140	0.021 ± 0.002
	124	1.07 ± 0.63		* 141	0.0016 ± 0.0001
	125	3.05 ± 1.34		* 142	0.00009 ± 0.00001

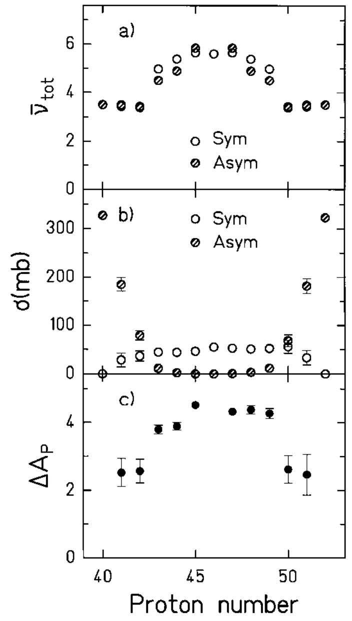

Fig. 14. **a** Mean total number $\bar{\nu}_{tot}$ of evaporated neutrons for the symmetric (*open points*) and asymmetric (*hatched points*) modes of fission. **b** Contribution of the two modes in secondary distributions for the elements Zr to Te. **c** Distance in mass units between the most probable masses linked to the two modes

between the scission configuration and the ground state of the final fragments at infinity. In addition an intrinsic excitation energy E_{int} contributes which results from a dissipative coupling between collective and single-particle degrees of freedom during the descent from the saddle to scission points. For ^{235}U(n$_{th}$,f), the difference between the mean evaporated neutron number for the Zr/Te and Pd/Pd pairs is interpreted by the different deformation energies at the scission point linked to the different fission modes: a heavy near spherical nucleus and its light deformed partner compared to a symmetric elongated configuration of two nuclei. Since the GDR excitation dominates the production of the Zr/Te pair, the fissioning nucleus receives an energy excess of 6 MeV compared to thermal neutron-induced fission. These additional 6 MeV are converted into E_{int} and may increase the viscosity between saddle and scission. Finally the Zr and Te isotopes show an increased excitation energy of 10 MeV more compared to the one obtained in ^{235}U(n$_{th}$,f) as deduced from $\bar{\nu}_{tot}$-values. The excitation energy excess in the Pd isotopes is found larger (13 MeV), which reflect the larger energy in the entrance channel caused by the DGDR and nuclear interactions.

Figure 14b presents the cross sections for the modes of symmetric and asymmetric fission. It clearly shows that at Z=50 the mode of asymmetric fission decreases and the mode of symmetric fission increases going from the peaks towards the valley of the distribution. The available energy at the saddle point increases the intrinsic energy E_{int}. This increase damps shell effects and favours the liquid drop behaviour, that means symmetric scission configurations. This could explain our finding of a large component linked to the symmetric fission mode even in the Sn and Sb isotopes.

The distance ΔA_P between the most probable masses linked to the two modes is displayed in Fig. 14c. It reaches 4.3±0.1 amu in the valley and 2.6±0.2 amu for Z=50-51 and their partner. These absolute values and the sharp transition of ΔA_P-values around Z=50 directly depend on the excitation energy value put in the calculation of $\bar{\nu}(A)$. It is noteworthy that ΔA_P=4 was found as well for the In isotopes in the ^{235}U(n_{th},f) reaction [41].

Table 5. Fit parameters for secondary isobaric distributions: mass yields $Y(A)$, most probable charge values Z_P and charge dispersions σ_Z

A	Y(A) (%)	Z_P	σ_Z	A	Y(A) (%)	Z_P	σ_Z
85	1.92± 0.20	33.8 ± 0.1	0.72 ± 0.03	110	0.77± 0.05	43.7 ± 0.1	0.67 ± 0.01
86	1.96± 0.09	34.4 ± 0.1	0.69 ± 0.02	111	0.75± 0.04	44.2 ± 0.1	0.67 ± 0.01
87	2.35± 0.11	34.9 ± 0.1	0.67 ± 0.02	112	0.80± 0.04	44.5 ± 0.1	0.69 ± 0.01
88	2.89± 0.14	35.3 ± 0.1	0.64 ± 0.01	113	0.84± 0.04	45.0 ± 0.1	0.68 ± 0.01
89	3.50± 0.18	35.7 ± 0.1	0.64 ± 0.01	114	0.88± 0.04	45.4 ± 0.1	0.66 ± 0.01
90	4.05± 0.21	36.0 ± 0.1	0.63 ± 0.01	115	0.92± 0.04	45.8 ± 0.1	0.65 ± 0.01
91	4.34± 0.24	36.4 ± 0.1	0.62 ± 0.01	116	0.95± 0.04	46.1 ± 0.1	0.67 ± 0.01
92	4.37± 0.26	36.8 ± 0.1	0.63 ± 0.01	117	0.93± 0.04	46.4 ± 0.1	0.61 ± 0.01
93	4.57± 0.26	37.2 ± 0.1	0.62 ± 0.01	118	0.90± 0.04	46.8 ± 0.1	0.61 ± 0.01
94	5.06± 0.28	37.6 ± 0.1	0.62 ± 0.01	119	0.84± 0.04	47.2 ± 0.1	0.62 ± 0.01
95	5.20± 0.27	37.9 ± 0.1	0.62 ± 0.01	120	0.79± 0.04	47.5 ± 0.1	0.62 ± 0.01
96	5.39± 0.26	38.3 ± 0.1	0.62 ± 0.01	121	0.71± 0.04	47.8 ± 0.1	0.57 ± 0.01
97	5.31± 0.26	38.7 ± 0.1	0.62 ± 0.01	122	0.69± 0.04	48.2 ± 0.1	0.58 ± 0.01
98	5.39± 0.22	39.1 ± 0.1	0.64 ± 0.01	123	0.74± 0.05	48.6 ± 0.1	0.58 ± 0.01
99	5.57± 0.18	39.5 ± 0.1	0.64 ± 0.01	124	0.70± 0.05	48.8 ± 0.1	0.55 ± 0.01
100	5.74± 0.12	39.8 ± 0.1	0.64 ± 0.01	125	0.60± 0.05	49.0 ± 0.1	0.58 ± 0.01
101	5.69± 0.15	40.2 ± 0.1	0.65 ± 0.01	126	0.56± 0.06	49.4 ± 0.1	0.58 ± 0.01
102	5.09± 0.19	40.6 ± 0.1	0.65 ± 0.01	127	0.75± 0.13	49.7 ± 0.1	0.59 ± 0.03
103	4.26± 0.22	40.9 ± 0.1	0.67 ± 0.01	128	1.19± 0.16	50.0 ± 0.1	0.61 ± 0.02
104	3.38± 0.21	41.3 ± 0.1	0.69 ± 0.01	129	1.94± 0.22	50.4 ± 0.1	0.60 ± 0.01
105	2.21± 0.18	41.7 ± 0.1	0.68 ± 0.02	130	2.61± 0.29	50.7 ± 0.1	0.64 ± 0.02
106	1.23± 0.11	42.0 ± 0.1	0.68 ± 0.01	131	3.48± 0.28	51.0 ± 0.1	0.63 ± 0.02
107	0.86± 0.07	42.5 ± 0.1	0.69 ± 0.01	132	4.47± 0.22	51.4 ± 0.1	0.62 ± 0.02
108	0.82± 0.06	42.9 ± 0.1	0.68 ± 0.01	133	5.18± 0.16	51.7 ± 0.1	0.59 ± 0.02
109	0.81± 0.05	43.3 ± 0.1	0.67 ± 0.01	134	5.11± 0.21	51.9 ± 0.1	0.58 ± 0.03

5 Some characteristics of the low-energy fission component

In the following, we shall consider the variables usually studied in low-energy fission. When it is possible, the fission modes will be separately treated.

5.1 Relative independent mass yields

Figure 15 presents the isobaric yields $Y(A)$ after neutron emission. A periodic structure of 5-6 mass units related to the preponderance of even elements in isobaric distributions is clearly exhibited for the peak of light isotopes. The fit of the mass distribution by means of a superposition of Gaussian curves allows to assign mass regions where the fission modes Standard I (SI), Standard II (SII) and Super-Long (SL) [12] dominate the yields. The strength, mean mass and variance of each mode are presented in Table 6 and main isotopes of each of the modes are deduced in Table 7. The position of the SI and SII channels are in agreement with ^{238}U(γ, f) experiments [42]. The primary neutron numbers for the corresponding heavy fragments are N=82 and N=88, the spherical and deformed neutron shell of [11]. The larger contribution of the SL-channel compared to other data obtained in the excitation energy regime around 10 MeV reinforces our assumption of two energy domains. The peak-to-valley ratio, defined by the ratio between the yields in the SI and SII channels and the yields in the SL channel, is 6.3±1.0. This value is consistent with the values extracted from the Z-distribution: a value of 5.8±1.0 was found for the total distribution and 7.1±1.0 for the electromagnetic part. A mean excitation energy of about 20 MeV in the entrance channel is confirmed for events leading to symmetric configurations [6].

Table 6. Contribution of the fission modes to the mass distribution of light isotopes (mass yield, mean mass and width)

Fission mode	Yield (%)	A_L	σ_m
SI	16 ± 4	101.3 ± 0.1	2.3 ± 0.2
SII	70 ± 3	94.3 ± 0.4	6.0 ± 0.3
SL	14 ± 2	116.3 ± 0.3	6.4 ± 0.7

It is noteworthy that the SI-channel still carries 18% of the asymmetric fission yields for excitation energies around 12 MeV. This was already seen in the mass distribution measured for ^{238}U(p, f) at 13.9 MeV excitation energy [43]. The strength of the SI channel appears in the isotopic distributions for elements from In to Te. Indeed, the higher measured yields linked to the N=82 shell are clearly shown in Fig. 16a. Gaussian curves were used to fit the cross sections without taking into account the N=82 points. The difference between the cross sections deduced from the fit and the measured cross sections are given in Table 8. The largest yield excess at N=82 is found for Sn (67±20%). The same procedure was used to extract an excess of yields linked to Z=50 in isotonic distributions (see

Table 7. Calculation of the primary distinguished isotopes for each fission mode by means of $A'_L = A_L + \bar{\nu}(A_L)$, $A'_H = A_0 - A'_L$, $Z_H = Z_{UCD} + \delta Z$. The SL mode leads to symmetric configurations for Pd isotopes: $Z_L = Z_H = 46$ and $A'_L = A'_H = \frac{A_0}{2}$. The discrepancies with expected values (*last column*) indicate the limit of accuracy of our method

	A'_L	A'_H	Z_L	Z_H	N'_H	
SI	103.3 ± 0.3	134.5 ± 0.5	40.3 ± 0.2	51.7 ± 0.2	82.9 ± 0.7	$^{134}_{82}$Te / $^{104}_{64}$Zr
SII	95.9 ± 0.6	142.0 ± 0.8	37.7 ± 0.3	54.3 ± 0.3	87.6 ± 1.1	$^{142}_{88}$Xe / $^{96}_{58}$Sr
SL	119.3 ± 0.5	117.9 ± 0.7	46.3 ± 0.3	45.7 ± 0.3	72.2 ± 1.0	$^{119}_{73}$Pd / $^{119}_{73}$Pd

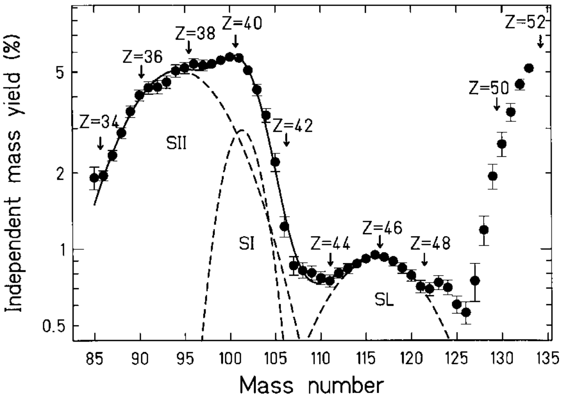

Fig. 15. Mass distribution for mass numbers 85 to 134. The *arrows* indicate the masses for which the isobaric distributions are dominated by even Z values. The *dashed lines* show the contribution of the fission channels (SI, SII and SL) for the light fragments [12]. The *full line* represents the superposition of these three channels

Fig. 16b). Numbers given in Table 8 do not take into account the proton odd-even effect. The largest yield excess at Z=50 is found for the N=82 isotones (138±81%). However, absolute cross sections confirm early experiments [44] and the calculation of Wilkins et al [11] which show that the ^{132}Sn production is hindered by the charge polarization in the break-up at scission. Indeed, the A/Z-value of ^{134}Te is closer to the charge density of the fissioning nucleus than the A/Z-value of ^{132}Sn. ^{134}Te is produced 6.5 times more abundantly than ^{132}Sn in this experiment. The persistence of the N=82 and Z=50 closed shell effects proves that the neighbouring isotopes were formed from a weakly excited U isotope. Indeed, yield enhancements of closed-shell spherical nuclei are found to disappear at an excitation energy of about 15 MeV in fusion [45] and fission [46].

5.2 Total kinetic energy distribution

The total kinetic energy (TKE) released in the fission of actinides depends on the mass asymmetry of the break-up. It is related to the deformation of the two nascent fragments: low $\alpha_L+\alpha_H$ values (α measures the quadrupole deformation) lead to high Coulomb energy and consequently high TKE-values. The scission-point models reproduce a well-known experimental result: the highest TKE-values are linked to the compact configurations with the heavy fragment around N=82. In Fig. 17, the TKE-values are calculated from

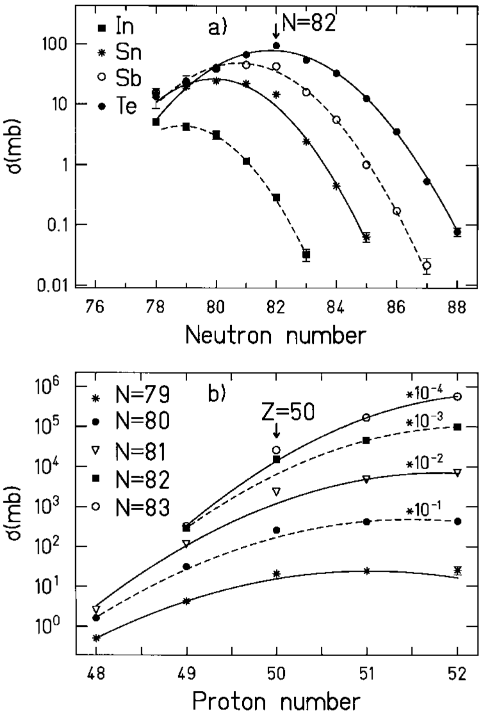

Fig. 16. **a** The N=82 closed shell effect in the measured isotopic distributions for In, Sn, Sb, Te and the associated fits. **b** The Z=50 closed shell effect in the N=79 to N=83 measured isotonic distributions and the associated fits

Table 8. Left part: Yield excess in the isotopic distributions for elements In to Te linked to the neutron shell N=82. Right part: Yield excess in the isotonic distributions for N=79 to N=83 linked to the proton shell Z=50. Values result from the substraction between measured values and Gaussian fit values. The large given errors directly come from this substraction procedure

Z	Yield excess of N=82 (%)	N	Yield excess of Z=50 (%)
49	11 ± 70	79	34 ± 37
50	67 ± 21	80	52 ± 25
51	30 ± 7	81	94 ± 39
52	30 ± 11	82	138 ± 81
		83	87 ± 118

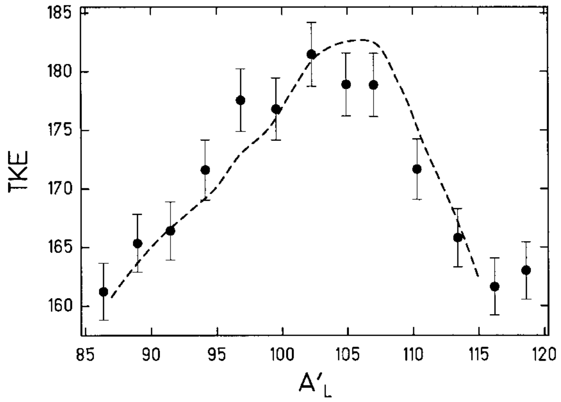

Fig. 17. Average total kinetic energy versus primary mass number. The *dashed line* represents the values measured in the ^{235}U(n$_{th}$, f) reaction [20]. Those TKE and A'-values are multiplied by a factor $\frac{238}{236}$ to make the comparison easier

$$\begin{cases} TKE(Z)_{/MeV} = \frac{931}{2} A'_P(Z) {\beta_F}^2(Z) \frac{A_0}{A_0 - A'_P(Z)} \\ \qquad for\ Z = 34 - 39 \\ TKE(Z)_{/MeV} = \frac{931}{2} (A'_P(Z) {\beta_F}^2(Z) \\ \qquad + A'_P(92 - Z) {\beta_F}^2(92 - Z)) \\ \qquad for\ Z = 40 - 46 \end{cases}$$

with β_F the velocity of the fragment A'_P in the center of mass system.

It is difficult to obtain accurate data on the velocity and TKE in measurements using inverse kinematics. The accuracy of the TKE-values in our measurement is not better than ±3 MeV. Figure 17 shows a dependence similar to the distribution measured in thermal neutron-induced fission of ^{235}U for the asymmetric configurations. It is also consistent with results obtained in ^{238}U(γ, f) [42] and in ^{238}U($\alpha, \alpha' f$) [47] for neighbouring excitation energies. The SII-mode, dominating the production of elements Z=36-39, presents an average TKE around 172 MeV. The SI-mode is found for elements Z=40-41 at a TKE of 180 MeV. The SL-mode at Z=44-46 gives TKE≃164 MeV. We confirm that the SI-mode is the most compact configuration, the SII-mode is less compact and the SL-mode shows the most elongated scission configurations. In ^{235}U(n$_{th}$, f) a TKE-value around 150 MeV was observed for symmetric fission [48]. Our value around 164 MeV indicates that increasing the excitation energy of the fissioning system to 20 MeV reduces the elongation of the scission configuration.

5.3 Odd-even effects

The charge distribution displayed in Fig. 8 shows a well pronounced odd-even effect in the peaks but none in the valley. Assuming the Z-distribution to be a Gaussian below Z=42, a quantitative measurement of the local proton odd-even effect was obtained with the method of differences as described in [24] (Fig. 18). The values of 6% to 10% suggest an excitation energy around 10 MeV which is one of the strongest argument for a large contribution of the GDR to fission leading to these asymmetric fragmentations.

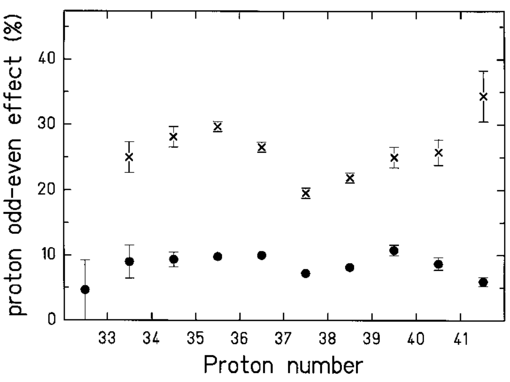

Fig. 18. Local proton odd-even effect versus proton number for this experiment (*full points*) and ^{235}U(n$_{th}$, f) (*crosses*) [20]

Unlike the proton odd-even effect which reflects directly the charge split, the neutron odd-even effect is widely influenced by neutron evaporation. The local neutron odd-even effect for each element, considering only the isotopes populating the fission peaks, was found to be small and of the same order than the one measured by Lang et al for ^{235}U(n$_{th}$,f) [20].

5.4 The mass-and-charge distribution mechanism

The partition of the mass and charge between the fission fragments before evaporation of post-scission neutrons is analysed by the quantities $\delta A'(Z)$ and $\delta Z(A')$ [23].

$$\delta A'(Z) = (A'_P - A'_{UCD})_H = (A'_{UCD} - A'_P)_L \qquad (4)$$

measures for an isotopic distribution the deviation of the average primary mass from the $A'_{UCD} = \frac{Z}{92} A_0$ value predicted by the "Unchanged Charge Density" hypothesis. A_0, the mean mass of the fissioning nucleus, is taken as 237.8 for Z=34-42 and 237.2 for Z=43-46. Figure 19a presents the measured $\delta A'$-values compared to results obtained in ^{235}U(n$_{th}$,f) reactions. A value of 1.10±0.16 and 0.99±0.16 was found for Rb isotopes in fission of ^{238}U induced by 40 and 60 MeV protons, respectively [24]. The rather constant values observed around the asymmetric fission peaks (SII-mode) confirm that the polarization varies slowly with the energy deposited in the fissioning nucleus. The fission modes are treated separately in this Fig.. The SII-mode (Z≃53-58) and the mixing of SI and SII-modes (Z≃50-52) give values around 1.5 mass units. The sudden change between Z=49 and 50 reflects the abrupt frontier between the two excitation energy domains: 20 MeV between Z=43-49, 12 MeV elsewhere. Even if the absolute values are questionable, it is obvious that the asymmetric mode gives rise to larger $\delta A'$ values for Z=47-49 related to the influence of the scission configuration of the SI mode which is dominated by the strong shell corrections around N=82 and Z=50. On the contrary, the

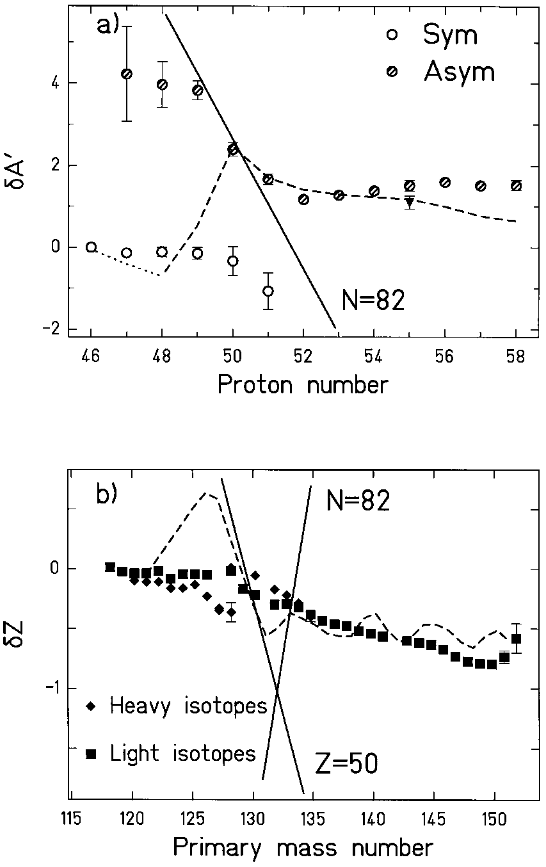

Fig. 19. **a** Mass difference $\delta A' = (A'_P - A'_{UCD})_H = (A'_{UCD} - A'_P)_L$ for isotopic distributions versus charge number. For elements Ag to Sb (and their charge partner), the symmetric (*open points*) and asymmetric (*hatched points*) fission modes were separately treated. The *dashed line* gives a fit to ^{235}U(n$_{th}$,f) and the *dotted line* gives an estimate for this last reaction [23]. The *full triangle* shows the $\delta A'$-value measured for Rb isotopes in fission of ^{238}U induced by 60 MeV protons [24] and the *full line* indicates the line N=82. **b** Charge polarization $\delta Z = (Z_P - Z_{UCD})_H = (Z_{UCD} - Z_P)_L$ for isobaric distributions versus primary mass number for light (*squares*) and heavy (*diamonds*) isotopes. The dashed line gives a fit to ^{235}U(n$_{th}$,f) and the full lines indicate the lines Z=50 and N=82

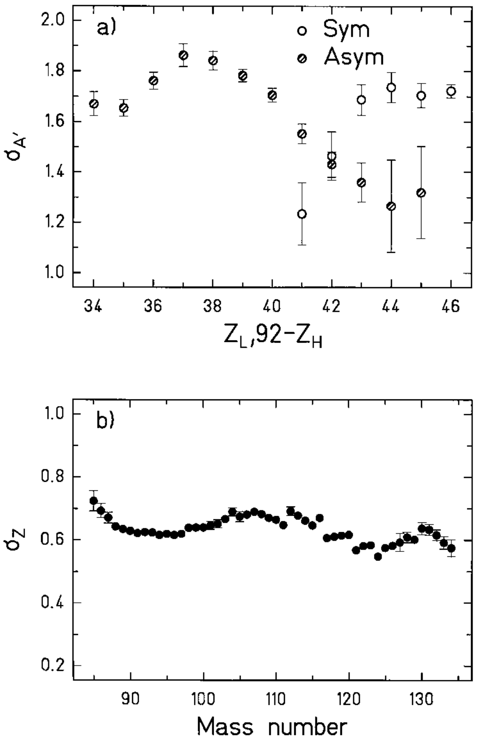

Fig. 20. **a** Standard deviation $\sigma_{A'}(Z)$ of the isotopic primary mass distribution versus proton number. For elements Nb to Rh, the symmetric (*open points*) and asymmetric (*hatched points*) fission modes were separately treated. **b** Standard deviation $\sigma_Z(A)$ of the post-neutron emission isobaric charge distribution versus mass number

symmetric fission mode produces nuclei not far from the UCD assumption.

From the most probable charge value Z_P of the isobaric distributions, the "charge polarization" $\delta Z(A')$ was extracted:

$$\delta Z(A') = (Z_P - Z_{UCD})_H = (Z_{UCD} - Z_P)_L \qquad (5)$$

$Z_{UCD} = 92\frac{A'}{A_0}$ is the charge value calculated by the "Unchanged Charge Density" hypothesis with $A' = A + \bar{\nu}(A)$. A_0 and $\bar{\nu}(A)$ are computed with the following assumption: 20 MeV excitation energy for 106<A<128 and 12 MeV elsewhere. The result is shown in Fig. 19b. The $\delta Z(A')$-values are strongly affected by these arbitrary limits between the excitation energy regimes for heavy masses around Z=50: they vary up to 0.5 charge unit due to the rapid change of $\bar{\nu}(A)$ with the excitation energy in this region. The influence of the Z=50 shell on charge polarization, which was predicted by Nörenberg [49] and established in thermal neutron-induced fission of ^{233}U [50] and ^{235}U [40], is not so pronounced here. This can be explained by the mixing of the asymmetric and symmetric fission modes in the isobaric distributions and by the larger yields for the symmetric mode, which suppress the influence of the Z=50 nuclear structure effects.

5.5 The mean mass-and-charge dispersion

Figure 20 displays the primary isotopic mass width $\sigma_{A'}(Z)$ and the isobaric charge width σ_Z(A) extracted from Tables 2 and 5, respectively. The σ_Z mean value is 0.531±0.004 for ^{235}U(n$_{th}$,f) [23]. Our values, systematically larger, are in agreement with results obtained in reactions where the excitation energy was around 10-15 MeV [43,51]. Whereas the slight broadening of the isobaric distributions with excitation energy can be affected by the evaporation of post-scission neutrons [20], the $\sigma_{A'}$-values reflect the mass dispersion linked to the fission process only. For elements lighter than Nb the primary isotopic distributions are larger than those of ^{235}U(n$_{th}$,f) for which a value of $\sigma_{A'}$=1.50±0.01 is given [23]. Moreover, the presented widths are close to the value of σ_A=1.818±0.002, after neutron evaporation, measured for Rb isotopes in fission of ^{238}U induced by 40 MeV protons [24]. The mass dispersion varies slowly with the excitation energy in the peak of light isotopes. The situation is more complicated in the transition domains between the peaks and the valley. Whereas the symmetric fission mode leads to a $\sigma_{A'}$-value around 1.7, comparable to the values in the peaks, the asymmetric mode is compatible with much lower isotopic widths around 1.5 for Sb and 1.3 for Ag.

6 The production of exotic nuclei

As already mentioned, more than 50 new neutron-rich nuclei were identified in this experiment (Fig. 10) [5]. More recently a new experiment performed with a beam intensity of 10^7/s on 1 g/cm^2 Be target revealed more than 70 new isotopes more ranging from Ca (Z=20) to Nd (Z=60) (see Fig. 10 for Z=31-52) [26,27]. Among these new species, extremely neutron-rich isotopes in the Co-Ni-Cu region were discovered including the double-magic ^{78}Ni [52]. The main reason for our observation of many new fragments is the inverse kinematics by which the transmission is increased by 5 orders of magnitude as compared to recoil separation in thermal neutron-induced fission [20]. Fig. 7 compares the measured isotopic distributions with a Pb target with normalized distributions obtained for ^{235}U(n$_{th}$,f) [21,23] and for reactions with excitation energies of few MeV above the fission barrier [24,25].

For the elements Br to Zr, the broadening of the isotopic distributions, combined with nearly the same A_P-values as found in thermal neutron-induced fission, leads to larger fractional independent isotopic yields $\frac{Y(Z,A)}{Y(Z)}$ for neutron-rich isotopes. If still more excitation energy is deposited in the system, the loss of neutrons is no longer compensated by this slightly wider distribution, as demonstrated for Rb isotopes [24]. The excitation energy window available to produce exotic nuclei is rather narrow. We estimate it from 6 to 25 MeV.

The enhancement with the excitation energy of the elemental yields in the symmetric region Z=43-49 was already used to identify new species [53]. Altogether the two experiments (with a Pb and Be target) push the frontier of known nuclei by up to 6 new isotopes. The symmetric region shows increased σ_A-values and no charge polarization.

The presence of the asymmetric fission mode nearly down to the bottom of the valley (Fig. 13) explains the yields of the In, Cd and even Ag neutron-rich isotopes. However, the small mass dispersion of this mode (see Fig. 20) leads to a sharp descent at the neutron-rich side of the isotopic distributions which cannot be compensated by the large mass polarization. The search of closed shell N=82 nuclei in this region suffers from this steep decrease, as demonstrated by the failure of search experiments for ^{129}Ag [54].

Compared to thermal neutron-induced fission, measured $\frac{Y(Z,A)}{Y(Z)}$-values of neutron-rich isotopes are larger for the elements Nb, Mo and Tc. They benefit twice: the symmetric fission mode is characterized by large mass dispersions and very small charge polarization. The distributions are pushed towards large A/Z-values.

The measured elemental yields of very asymmetric fission are higher compared to those obtained in thermal neutron-induced fission. As seen from Fig. 8 they are most favoured using a Be target instead of a Pb target and elements below Cu are produced by nuclear fission only. Going from the smaller excitation energies in GDR fission (around 12 MeV) to the larger energies in nuclear fission (20-30 MeV) broadens the mass distribution. In order to produce isotopes of lighter elements higher excitation energies might be useful, but to synthesize the most neutron-rich isotopes of these elements again a narrow energy window of 20-30 MeV will be optimal. The very asymmetric fission mode giving nuclei around ^{78}Ni will be studied in detail in a forthcoming paper [55].

7 Conclusion

In the present work the low-energy fission of 750 AMeV ^{238}U-ions interacting with a Pb target is analysed in detail. For the first time by inverse kinematics all isotopes produced in fission can be separated. Cross sections of more than 250 nuclei were deduced from velocity distributions. Isotopic distributions were given for elements Ga to Te. Using the rich information accumulated in 50 years of previous work in fission, we were able to disentangle the low-energy fission from higher energy fission and to derive the characteristics of different fission modes.

The mean mass values of isotopic distributions for elements populating the light fission peak (Z=34-39) were found consistent with the hypothesis of dominant GDR excitation (around 12 MeV) via the virtual photon spectrum. This average energy is in agreement with the measured proton odd-even effect. However, isotopic distributions exhibit a mixture with higher-energy fission events for very asymmetric mass ratios and for elements which populate the valley. The peak-to-valley ratio suggests that symmetric fission events result from a fissioning U isotope sustaining about 20 MeV of excitation energy. These fission events follow electromagnetic excitation of higher giant resonances, as GQR and eventually DGDR, or soft nuclear interactions. For elements (Z=41-51), the contribution of the low-energy fission in the isotopic distributions was extracted by using the complementary isotopic distributions of their charge partner. The reconstructed distributions clearly show the competition between the symmetric and asymmetric fission modes proposed in the frame of static scission point models. The ratio of the symmetric to the asymmetric modes in the isotopic distributions slowly decreases from Z=46 to Z=51. The presence of the symmetric fission mode in the Z=49-51 distributions (and their charge partner) reinforces the assumption of an excitation energy component larger than the GDR energy. The mean number of post-scission neutrons evaluated for a given charge pair, suggests an excitation energy excess of 10-13 MeV in the fission fragments compared to ^{235}U(n$_{th}$,f). A part of this energy excess could be understood by an increased viscosity between saddle and scission for higher excitation energies in the entrance channel.

The SI, SII and SL fission modes are clearly exhibited in the mass distribution with a significant participation of the spherical closed shells N=82, Z=50 and the deformed shell at N=88. The increased large yields linked to spherical closed shells compared to neighbouring isotopes is consistent with a low-energy process. The mean total kinetic energy, determined for each Z-splitting, was found to be close to the one measured for ^{235}U(n$_{th}$,f). The primary mass dispersion and the charge polarization were deduced from reconstructed isotopic distributions for both the asymmetric and symmetric modes. The polarization in the peaks of the mass distribution was not found to be very sensitive to the excitation energy deposited in the entrance channel. The symmetric and asymmetric fission modes lead to a different N/Z partition: an UCD behaviour for the elements in the valley and mean A/Z-values larger than the one of ^{238}U for heavier elements, reflecting the strong influence of the N=82 and Z=50 shells. The variance of the primary isotopic distributions is found around 1.7 except for the asymmetric fission mode extending into the valley where it is slightly smaller. This value confirms that the width of the isotopic distributions varies slowly with the excitation energy.

The fission yields of neutron-rich isotopes compared to thermal neutron-induced fission are larger in the excitation energy range of 10-30 MeV. Neutron-rich isotopes in the valley and from very asymmetric break-up become accessible for further studies. Altogether 117 new neutron-rich isotopes were identified in the two experiments up to cross sections of less than one nb. Secondary beams of these isotopes will allow to measure masses and halflives and to perform first spectroscopic studies.

We want to thank the SIS-accelerator group for having provided the first ^{238}U beam which started fission physics at the new GSI-machines. We all thank K.H. Schmidt and his group for their contribution to the experimental equipment at the FRS, which allowed to perform the reported experiment. Two of us, S. Czajkowski and C. Donzaud, want to thank for having been invited as GSI-guest scientists.

References

1. Polikanov, S., Brüchle, W., Folger, H., Jäger, E., Krogulski, T., Schädel, M., Schimpf, E., Wirth, G., Aumann, T., Kratz, J.V., Stiel, E., Trautmann, N.: Z. Phys. A**350**, 221 (1994)
2. Hesse, M., Bernas, M., Armbruster, P., Aumann, T., Czajkowski, S., Dessagne, Ph., Donzaud, C., Geissel, H., Hanelt, E., Heinz, A., Kozhuharov, C., Miehe, Ch., Münzenberg, G., Pfützner, M., Röhl, C., Schmidt, K.-H., Schwab, W., Stéphan, C., Sümmerer, K., Tassan–Got, L.: Z. Phys. A**355**, 69 (1996)
3. Schmidt, K.-H., Heinz, A., Clerc, H.-G., Blank, B., Brohm, T., Czajkowski, S., Donzaud, C., Geissel, H., Hanelt, E., Irnich, H., Itkis, M.C., De Jong, M., Junghans, A., Magel, A., Münzenberg, G., Nickel, F., Pfützner, M., Piechaczek, A., Röhl, C., Scheidenberger, C., Schwab, W., Steinhäuser, S., Sümmerer, K., Trinder, W., Voss, B., Zhdanov, S.V.: Phys. Lett B**325**, 313 (1994)
4. Rubehn, Th., Müller, W.F.J., Bassini, R., Begemann-Blaich, M., Blaich, Th., Ferrero, A., Groß, C., Imme, G., Iori, I., Kunde, G.J., Kunze, W.D., Lindenstruth, V., Lynen, U., Moroni, A., Möhlenkamp, T., Moretto, L.G., Ocker, B., Pochodzalla, J., Raciti, G., Sann, H., Schüttauf, A., Seidel, W., Serfling, V., Trautmann, W., Trzcinski, A., Verde, A., Wörner, A., Zude, E., Zwieglinski, B.: Z. Phys. A**353**, 197 (1995)
5. Bernas, M., Czajkowski, S., Armbruster, P., Geissel, H., Dessagne, Ph., Donzaud, C., Faust, H.-R., Hanelt, E., Heinz, A., Hesse, M., Kozhuharov, C., Miehe, Ch., Münzenberg, G., Pfützner, M., Röhl, C., Schmidt, K.-H., Schwab, W., Stéphan, C., Sümmerer, K., Tassan-Got, L., Voss, B.: Phys. Lett. B**331**, 19 (1994)
6. Armbruster, P., Bernas, M., Czajkowski, S., Geissel, H., Aumann, T., Dessagne, Ph., Donzaud, C., Hanelt, E., Heinz, A., Hesse, M., Kozhuharov, C., Miehe, Ch., Münzenberg, G., Pfützner, M., Schmidt, K.-H., Schwab, W., Stéphan, C., Sümmerer, K., Tassan-got, L., Voss, B.: Z. Phys. A**355**, 191 (1996)
7. Schmidt, K.-H., Brohm, T., Clerc, H.-G., Dornik, M., Fauerbach, M., Geissel, H., Grewe, A., Hanelt, E., Junghans, A., Magel, A., Morawek, W., Münzenberg, G., Nickel, F., Pfützner, M., Scheidenberger, C., Sümmerer, K., Vieira, D., Voss, B., Ziegler, C.: Phys. Lett. B**300**, 313 (1993)
8. Hilscher, D., Rossner, H., Ann. de Phys. Fr. **17**, 471 (1992)
9. Meitner, L.: Nature, (London) **165**, 561 (1950)
10. Turkevich, A., Niday, J.B.: Phys. Rev. **84**, 52 (1951)
11. Wilkins B. D., Steinberg, E. P., Chasman, R. R.: Phys. Rev. C**14**, 1832 (1976)
12. Brosa, U., Grossmann, S., Müller, A.: Phys. Reports **197**, 167 (1990)
13. Ziegler, C., Brohm, T., Clerc, H.-G., Geissel, H., Schmidt, K.-H., Sümmerer, K, Vieira, D.J., Voss, B.: GSI, Scientific–Report, 91–1 (1990) 291
14. Clerc, H.-G., De Jong, M., Brohm, T., Dornik, M., Grewe, A., Hanelt, E., Heinz, A., Junghans, A., Röhl, C., Steinhäuser, S., Voss, B., Ziegler, C., Schmidt, K.-H., Czajkowski, S., Geissel, H., Irnich, H., Magel, A., Münzenberg, G., Nickel, F., Piechaczek, A., Scheidenberger, C., Schwab, W., Sümmerer, K., Trinder, W., Pfützner, M., Blank, B., Ignatyuk, A., Kudyaev, G.: Nucl. Phys. A**590**, 785 (1995)
15. Geissel, H., Armbruster, P., Behr, K.H., Brünle, A., Burkhard, K.H., Chen, M., Folger, H., Franczak, B., Keller, H., Klepper, O., Langenbeck, B., Nickel, F., Pfeng, E., Pfützner, M., Roeckl, E., Rykaczewski, K., Schall, I., Schardt, D., Scheidenberger, C., Schmidt, K.-H., Schröter, A., Schwab, T., Sümmerer, K., Weber, M., Münzenberg, G., Brohm, T., Clerc, H.-G., Fauerbach, M., Gaimard, J.J., Grewe, A., Hanelt, E., Knödler, B., Steiner, M., Voss, B., Weckenmann, J., Ziegler, C., Magel, A., Wollnik, H., Dufour, J.P., Fujita, Y., Vieira, D.J.: Nucl. Instr. Meth. B**70**, 286 (1992)
16. Schwab, Th.: GSI–Rep. 91–10 (1991)

17. Pfützner, M., Geissel, H., Münzenberg, G., Nickel, F., Scheidenberger, C., Schmidt, K.-H., Sümmerer, K., Brohm, T., Voss, B., Bichsel, H.: Nucl. Inst. and Methods B**86**, 213 (1994)
18. Voss, B., Behr, K.-H., Brohm, T., Clerc, H.-G., Geissel, H., Grewe, A., Hanelt, E., Heinz, A., DeJong, M., Junghans, A., Magel, A., Morawek, W., Münzenberg, G., Nickel, F., Pfützner, M., Röhl, C., Sümmerer, K., Scheidenberger, C., Schmidt, K.-H., Steinhäuser, S., Ziegler, C: Nucl. Inst. and Meth. A**364**, 150 (1995)
19. Stelzer, H. : Nucl. Inst. and Meth A**310**, 103 (1991)
20. Lang, W., Clerc, H.-G., Wohlfarth, H., Schrader, H., Schmidt, K.-H.: Nucl. Phys. A**345**, 34 (1980)
21. Sida, J.L., Armbruster, P., Bernas, M., Bocquet, J.P., Brissot, R., Faust, H.R.: Nucl. Phys. A**502**, 233 (1989)
22. Belhadaf, D., Bocquet, J.P., Brissot, R., Ristori, Ch., Crançon, J., Nifenecker, H., Mougey, J., Ramamurthy, V.S.: Z. Phys. A**309**, 253 (1983)
23. Wahl, A.C.: Atomic Data and Nucl. Data Tables **39**, 1 (1988)
24. Tracy, B.L., Chaumont, J., Klapisch, R., Nitschke, J.M., Poskanzer, A.M., Roeckl, E., Thibault, C.: Phys. Rev. C**5**, 222 (1972)
25. Pommé, S., Jacobs, E., Persyn, K., De Frenne, D., Govaert, K., Yoneama, M.L.: Nucl. Phys. A**560**, 689 (1993)
26. Czajkowski, S., Ameil, F., Armbruster, P., Bernas, M., Dessagne, Ph., Donzaud, C., Engelmann, C., Faust, H.-R., Geissel, H., Hanelt, E., Heinz, A., Hesse, M., Kozhuharov, C., Miehe, Ch., Münzenberg, G., Pfützner, M., Röhl, C., Schmidt, K.-H., Schwab, W., Stéphan, C., Sümmerer, K., Tassan-Got, L., Voss, B.: in Proc. of the International Conference on Exotic Nuclei and Atomic Masses, Editions Frontieres p553 (1995)
27. Bernas, M., Armbruster, P., Czajkowski, S., Donzaud, C., Geissel, H., Ameil, F., Dessagne, Ph., Engelmann, C., Heinz, A., Janas, Z., Kozhuharov, C., Miehe, Ch., Münzenberg, G., Pfützner, M., Böckstiegel, C., Schmidt, K.-H., Schwab, W., Stéphan, C., Sümmerer, K., Tassan-Got, L., Voss, B.: Nucl. Phys. A**616**, 352 (1997)
28. Benesh, C.J., Cook, B.C. and Vary, J.P.: Phys. Rev. C**40**, 1198 (1989)
29. Aumann, T., Sümmerer, K., Geissel, H., Blank, B., Brohm, T., Clerc, H.-G., Czajkowski, S., Donzaud, C., Grewe, A., Hanelt, E., Heinz, A., Irnich, H., De Jong, M., Junghans, Kratz, J.V., A., Magel, A., Münzenberg, G., Nickel, F., Pfützner, M., Piechaczek, A., Röhl, C., Scheidenberger, C., Schmidt, K.-H., Schwab, W., Steinhäuser, S., Trinder, W., Voss, B.: Z. Phys. A**352**, 163 (1995)
30. Bertulani, C. A., Baur, G.: Nucl. Phys. A**442**, 739 (1985)
31. Caldwell, J. T. , Dowdy, E. J., Berman, B. L., Alvarez, R. A., Meyer, P.: Phys. Rev. C**21**, 1215 (1980)
32. Boikov, G.S., Dmitriev, V.D., Kudyaev, G.A., Ostapenko, Yu.B., Svirin, M.I., Smirenkin, G.N.: Z. Phys. A**340**, 79 (1991)
33. Schwab, W., et al: to be published in Eur. Phys. J A
34. Benlliure, J., et al: to be published in Eur. Phys. J A
35. Bishop, C.J., Vandenbosch, R., Aley, R., Shaw, R.W., Halpern, J. and I.: Nucl. Phys. A**150**, 129 (1970)
36. Strecker, M., Wien, R., Plischke, P., Scobel, W.: Phys. Rev. C**41**, 2172 (1990)
37. Cheifetz, E., Fraenkel, Z.: Phys. Rev. Lett. **21**, 36 (1968)
38. Burnett, S.C., Ferguson, R.L., Plasil, F., Schmitt, H.W.: Phys. Rev. C**3**, 2034 (1971)
39. Zöller, C.: Ph. D. Thesis, TH Darmstadt, 1995
40. Rudstam, G., Aagaard, P., Ekström, B., Lund, E., Göktürk, H., Zwicky, H.U.: Radiochimica Acta **49**, 155 (1990)
41. Wahl, A.C.: Los Alamos National Laboratory LA-UR-92-1425, Proc. of the Nuclear Energy Agency Nuclear Science Comittee Specialists' Meeting on Fission Product Nuclear Data, Japan 1992
42. Pommé, S., Jacobs, E., Piessens, M., De Frenne, D., Persyn, K., Govaert, K., Yoneama, M.L.: Nucl. Phys. A**572**, 237 (1994)
43. Yokoyama, A., Takahashi, N., Nitani, N., Baba, H., Kasuga, R., Yamaguchi, T., Yano, D., Takamiya, K., Shinohara, N., Tsukada, K., Hatsukawa, Y., Nagame, Y.: Z. Phys. A**356**, 55 (1996)
44. Strom, P.O., Love, D.L., Greendale, A.E., Delucchi, A.A., Sam, D., Ballou, N.E.: Phys. Rev. **144**, 984 (1966)
45. Schmidt, K.-H., Faust, W., Münzenberg, G., Reisdorf, W., Clerc, H.-G., Vermeulen, D., Lang, W.: in Physics and Chemistry of fission, Proc. Jülich, May 1979 (IAEA 1980)) vol. 1
46. Quade, U., Rudolph, K., Skorka, S., Armbruster, P., Clerc, H-G., Lang, W., Mutterer, M., Schmitt, C., Theobald, J.P., Gönnenwein, F., Pannicke, J., Schrader, H., Siegert, G., Engelhardt, D.: Nucl. Phys. A**487**, 1 (1988)
47. Back, B.B., Shotter, A.C., Symons, T.J.M., Bice, A., Gelbke, C.K., Awes, T.C., Scott, D.K.: Phys. Rev. C**23**, 1105 (1981)
48. Brissot, R., Bocquet, J.P., Ristori, C., Crançon, J., Guet, C.R., Nifenecker, H.A., Montoya, M., Proc. Jülich, May 1979 (IAEA 1980)) vol. 2
49. Nörenberg, W.: Z. Phys. **197**, 246 (1966)
50. Bocquet, J.P., Brissot, R.: Nucl. Phys. A**502**, 213 (1989)
51. De Frenne, D., Thierens, H., Proot, B., Jacobs, E., De Gelder, P., De Clercq, A., Westmeier, W.: Phys. Rev. C**26**, 1356 (1982)
52. Engelmann, Ch., Ameil, F., Armbruster, P., Bernas, M., Czajkowski, S., Dessagne, Ph., Donzaud, C., Geissel, H., Heinz, A., Janas, Z., Kozhuharov, C., Miehe, Ch., Münzenberg, G., Pfützner, M., Röhl, C., Schwab, W., Stéphan, C., Sümmerer, K., Tassan-Got, L., Voss, B.: Z. Phys. A**352**, 351 (1995)
53. Äystö, J., Astier, A., Enqvist, T., Eskola, K., Janas, Z., Jokinen, A., Kratz, K.L., Leino, M., Penttilä, H., Pfeiffer, B., Zylicz, J.: Phys. Rev. C**69**, 1167 (1992)
54. Fedoseyev, V.N., Jading, Y., Jonsson, O.C., Kirchner, R., Kratz, K.L., Krieg, M., Kugler, E., Lettry, J., Mehren, T., Mishin, V.I., Ravn, H.L., Rauscher, T., Scheerer, F., Tengblad, O., Van Duppen, P., Wöhr, A.: Z. Phys. A**353**, 9 (1995)
55. Engelmann, C., et al: Ph. D. Thesis in preparation, GSI, TH Darmstadt